

Gradient-Based Quantification of Epistemic Uncertainty for Deep Object Detectors

Tobias Riedlinger

Matthias Rottmann

Marius Schubert

Hanno Gottschalk

School of Mathematics and Natural Sciences
University of Wuppertal

{riedlinger, rottmann, mschubert, hgottsch}@uni-wuppertal.de

Abstract

The vast majority of uncertainty quantification methods for deep object detectors such as variational inference are based on the network output. Here, we study gradient-based epistemic uncertainty metrics for deep object detectors to obtain reliable confidence estimates. We show that they contain predictive information and that they capture information orthogonal to that of common, output-based uncertainty estimation methods like Monte-Carlo dropout and deep ensembles. To this end, we use meta classification and meta regression to produce confidence estimates using gradient metrics and other baselines for uncertainty quantification which are in principle applicable to any object detection architecture. Specifically, we employ false positive detection and prediction of localization quality to investigate uncertainty content of our metrics and compute the calibration errors of meta classifiers. Moreover, we use them as a post-processing filter mechanism to the object detection pipeline and compare object detection performance. Our results show that gradient-based uncertainty is itself on par with output-based methods across different detectors and datasets. More significantly, combined meta classifiers based on gradient and output-based metrics outperform the standalone models. Based on this result, we conclude that gradient uncertainty adds orthogonal information to output-based methods. This suggests that variational inference may be supplemented by gradient-based uncertainty to obtain improved confidence measures, contributing to down-stream applications of deep object detectors and improving their probabilistic reliability.

1. Introduction

Deep artificial neural networks (DNNs) designed for tasks such as object detection or semantic segmentation provide a probabilistic prediction on given feature data such

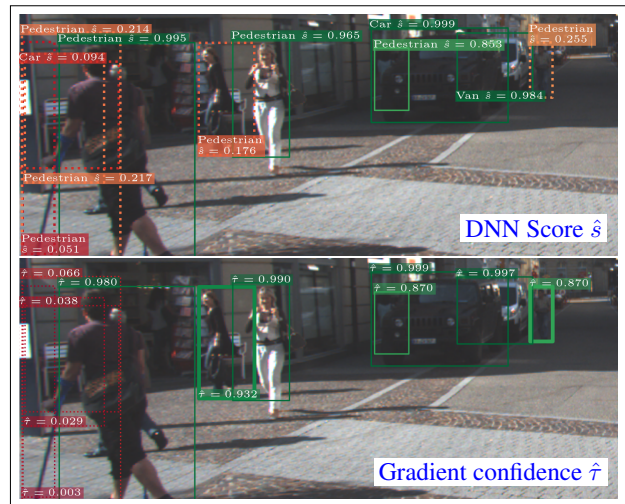


Figure 1. Object detection in a street scene (full images in Appendix E). Top coloration: Score \hat{s} ; bottom coloration: instance-wise gradient-based confidence $\hat{\tau}$ obtained by our method. Dashed boxes here indicate the discarding at any confidence threshold in $[0.3, 0.85]$. The top image contains FNs which are not separable from correctly discarded boxes based on the score (lower threshold would lead to FPs). In the bottom image, those \hat{s} -FNs are assigned higher confidences and there is a large range of thresholds with no FPs.

as camera images. Modern deep object detection architectures [1, 26, 28, 43, 44] predict bounding boxes for instances of a set of learned classes on an input image.

The so-called *objectness* or *confidence score* indicates the probability of the existence of an object for each predicted bounding box. Throughout this work, we will refer to this quantity which the DNN learns as the “score”. For applications of deep object detectors such as automated surgery or driving, the reliability of this component is crucial. See, for example the detection in the top panel of Fig. 1 where each box is colored from red (low score) to green

(high score). Apart from the accurate, green boxes, boxes with a score below 0.3 (dashed) contain true and false predictions which *cannot be reliably separated in terms of their score*. In addition, it is well-known that DNNs tend to give mis-calibrated scores [12, 13, 51] that are oftentimes overconfident and may also lead to unreliable predictions. Overconfident predictions might render an autonomous driving system inoperable by perceiving non-existent instances (false positives / FP). Perhaps even more detrimental, underconfidence may lead to overlooked (false negative / FN) predictions possibly endangering humans outside autonomous vehicles like pedestrians and cyclists, as well as passengers.

Apart from modifying and improving the detection architecture or the loss function, there exist methods to estimate prediction confidence more involved than the score in order to remedy these issues [30, 36, 48]. We use the term “confidence” more broadly than “score” to refer to quantities which represent the probability of a detection being correct. Such a quantity should reflect the model’s overall level of competency when confronted with a given input and is intimately linked to prediction uncertainty. Uncertainty for statistical models, in particular DNNs, can broadly be divided into two types [18] depending on their primary source [9, 20]. Whereas aleatoric uncertainty is mainly founded in the stochastic nature of the data generating process, epistemic uncertainty stems from the probabilistic nature of sampling data for training, as well, as the choice of model and the training algorithm. The latter is technically reducible by obtaining additional training data and is the central subject of our method.

Due to the instance-based nature of deep object detection, modern ways of capturing epistemic uncertainty are mainly based on the instance-wise DNN output. From a theoretical point of view, Bayesian DNNs [5, 33] represent an attractive framework for capturing epistemic uncertainty for DNNs by modeling their weights as random variables. Practically, this approach introduces a large computational overhead making its application infeasible for object detection. Therefore, in variational inference approaches, weights are sampled from predefined distributions to address this. These famously include methods like Monte-Carlo (MC) dropout [10, 50] generating prediction variance by performing several forward passes under active dropout. The same idea underlies deep ensemble sampling [25] where separately trained models with the same architecture produce variational forward passes. Other methods relying only on the classification output per instance can also be applied to object detection such as softmax entropy or energy score methods.

A number of other, strong uncertainty quantification methods that do not only rely on the classification output has also been developed for image classification architectures [4, 34, 40, 42]. However, the *transfer of such methods*

to object detection frameworks can pose serious challenges, if at all possible, due to architectural restrictions. For example, the usage of a learning gradient evaluated at the network’s own prediction was proposed [40] to contain epistemic uncertainty information for image classification and investigated for out-of-distribution (OoD) data. The method has also been applied gainfully to natural language understanding [53] where gradient metrics and deep ensemble uncertainty were aggregated to obtain well-calibrated and predictive confidence measures on OoD data. The epistemic content of gradient uncertainty has further been explored in [17] in the classification setting by observing shifts in the data distribution.

We propose a way to compute gradient features for the prediction of deep object detectors. We show that they perform on par with state-of-the-art uncertainty quantification methods and that they contain information that can not be obtained from output- or sampling-based methods. In particular, *we summarize our main contributions as follows:*

- We introduce a way of generating gradient-based uncertainty metrics for modern object detection architectures, allowing to generate uncertainty information from hidden network layers.
- We investigate the performance of gradient metrics in terms of meta classification (FP detection), calibration and meta regression (prediction of intersection over union *IoU* with the ground truth) and compare them to other means to quantify/approximate epistemic uncertainty and investigate mutual redundancy as well as detection performance through gradient uncertainty.
- We explicitly investigate the FP/FN-tradeoff for pedestrian detection based on the score and meta classifiers.
- We provide a theoretical treatment of the computational complexity of gradient metrics in comparison with MC dropout and deep ensembles and show that their FLOP count is similar at worst.

An implementation of our method will be made publicly available at <https://github.com/tobiasriedlinger/gradient-metrics-od>. A video illustration of our method is publicly available at <https://youtu.be/L4oVnQAGiBc>.

2. Related work

Epistemic uncertainty for deep object detection. Sampling-based uncertainty quantification such as MC dropout and deep ensembles have been investigated in the context of object detection by several authors in the past [14, 30, 35–37]. They are straight-forward to implement into any architecture and yield output variance for all bounding box features.

Harakeh *et al.* [14] employed MC dropout and Bayesian inference as a replacement of Non-Maximum Suppression

(NMS) to get a joint estimation of epistemic and aleatoric uncertainty.

Similarly, uncertainty measures of epistemic kind were obtained by Kraus and Dietmayer [23] from MC dropout. Miller *et al.* [36] investigated MC dropout as a means to improve object detection performance in open-set conditions. Different merging strategies for samples from MC dropout were investigated by Miller *et al.* [35] and compared with the influence of merging boxes in deep ensembles of object detectors [37]. It was found that even for small ensemble sizes, deep ensembles outperform MC dropout sampling. Lyu *et al.* [30] aggregated deep ensemble samples as if produced from a single detector to obtain improved detection performance. A variety of uncertainty measures generated from proposal box variance pre-NMS called MetaDetect was investigated by Schubert *et al.* [48]. In generating advanced scores and *IoU* estimates, it was reported that the obtained information is largely redundant with MC dropout uncertainty features but less computationally demanding. All of the above methods are based on the network output and generate variance in by aggregating prediction proposals in some manner. Moreover, a large amount of uncertainty quantification methods based on classification outputs can be directly applied to object detection [16, 29]. Little is known about other methods developed for image classification that are not directly transferable to object detection due to architectural constraints, such as activation-based [4] or gradient-based [40] uncertainty. The central difficulty in such an application lies in the fact that different predicted instances depend on shared latent features or DNN weights such that the base method can only estimate uncertainty for the entire prediction (consisting of all instances) instead of individual uncertainties for each instance. We show that gradient uncertainty information can be extracted from hidden layers in object detectors. We seek to determine how they compare against output-based methods and show that they contain orthogonal information.

Meta classification and meta regression. The term meta classification refers to the discrimination of TPs from FPs on the basis of uncertainty metrics which was first explored by Hendrycks and Gimpel [16] to detect OoD samples based on the maximum softmax probability.

Since then, the approach has been applied to natural language processing [53], semantic segmentation [2, 31, 45–47], instance segmentation in videos [32] and object detection [22, 48] to detect FP predictions on the basis of uncertainty features accessible during inference. Moreover, meta regression (the estimation of *IoU* based on uncertainty in the same manner) was also investigated [31, 32, 46–48] showing large correlations between estimates and the true localization quality.

Chan *et al.* [2] have shown that meta classification can be used to improve network accuracy, an idea that so-far

has not been achieved for object detection. Previous studies have overlooked class-restricted meta classification performance, *e.g.*, when restricting to safety-relevant instance classes. Moreover, in order to base downstream applications on meta classification outputs, resulting confidences need to be statistically reliable, *i.e.*, calibrated which has escaped previous research.

3. Gradient-based epistemic uncertainty

In instance-based recognition tasks, such as object detection or instance segmentation, the prediction consists of a list

$$\hat{y} = (\hat{y}^1, \dots, \hat{y}^{N_x}) \quad (1)$$

of instances (*e.g.*, bounding boxes). The length of \hat{y} usually depends on the corresponding input x and on hyperparameters (*e.g.*, confidence / overlap thresholds). Uncertainty information which is not generated directly from instance-wise data such as activation- or gradient-based information can *at best yield statements about the entirety of \hat{y}* but not immediately about individual instances \hat{y}^j . This issue is especially apparent for uncertainty generated from deep features which potentially all contribute to an instance \hat{y}^j . Here, we introduce an approach to generate gradient-based uncertainty metrics for the instance-based setting. To this end, we sketch how gradient uncertainty is generated for classification tasks.

Generically, given an input x , a classification network predicts a class distribution $\hat{y}(x, w) = (\hat{p}_1, \dots, \hat{p}_C)$ of fixed length C given a set of weights w . During training, the latter is compared to the ground truth label y belonging to x by means of some loss function $\mathcal{L}(\cdot, \cdot)$, which is minimized by optimizing w , *e.g.*, by standard stochastic gradient descent. The w -step is proportional to the gradient $g(x, w, y) := \nabla_w \mathcal{L}(\hat{y}(x, w); y)$ which can also be regarded as a measure of *learning stress* imposed upon w . Gradient uncertainty features are generated by substituting the non-accessible ground truth y with the network’s class prediction $\bar{y} := \arg \max_c \{\hat{p}_c\}_{c=1}^C$ and disregarding the dependence of the latter on w . In the following we will identify \bar{y} with its one-hot encoding. Scalar values are obtained by computing some magnitude of

$$g(x, w, \bar{y}) = \nabla_w \mathcal{L}(\hat{y}(x, w), \bar{y}). \quad (2)$$

To this end, in our experiments we employ the maps

$$\{\min(\cdot), \max(\cdot), \text{mean}(\cdot), \text{std}(\cdot), \|\cdot\|_1, \|\cdot\|_2\}. \quad (3)$$

We discuss the latter choice in our supplementary material and first illuminate a couple of points about the expression in Eq. (2).

Intuition and discussion of (2). First of all, Eq. (2) can be regarded as the *self-learning gradient* of the network. It,

therefore, expresses the learning stress on w under the condition that the class prediction \bar{y} were given as the ground truth label. The collapse of the (e.g., softmax) prediction \hat{y} to \bar{y} implies that (2) does not generally vanish in the classification setting. However, this consideration poses a problem for (bounding box) regression which we will address in the next paragraph. We also note that it is possible to generate fine-grained metrics by restricting w in (2) to sub-sets of weights w_ℓ , e.g., individual layers, convolutional filters or singular weights (computing partial gradients of \mathcal{L}).

Using Eq. (2) as a measure of uncertainty may be understood by regarding true and false predictions. A well-performing network which has \bar{y} already close to the true label y tends to experience little stress when trained on (x, y) with the usual learning gradient. This reflects *confidence* in the prediction \bar{y} and the difference between Eq. (2) and the true gradient is then small. In the case of false predictions $\bar{y} \neq y$, the true learning gradient enforces large adjustments in w . The self-learning gradient (2) behaves differently in that it is *large for non-peaked/uncertain* (high entropy) predictions \hat{y} and small for highly peaked distributions.

Extension to object detectors.

We first clarify the aforementioned complications in generating uncertainty information for object detection. Generally, the prediction (1) is the filtering result of a larger, often fixed number \hat{N}_{out} of output bounding boxes $\tilde{y}(x, w)$ (refer to Appendix A for details). Given a ground truth list y of bounding boxes, the loss function usually has the form

$$\mathcal{L} = \mathcal{L}(\tilde{y}(x, w); y), \quad (4)$$

such that all \hat{N}_{out} output bounding boxes potentially contribute to $g(x, w, y)$. Again, when filtering \tilde{y} to a smaller number of predicted boxes \hat{y} and converting them to ground truth format \bar{y} , we can compute the self-learning gradient $g(x, w, \bar{y})$. This quantity, however, does not refer to any individual prediction \hat{y}^j , but rather to all boxes in \bar{y} simultaneously. We take *two steps to obtain meaningful gradient information* for one particular box \hat{y}^j from this approach.

Firstly, we restrict the ground truth slot to only contain the length-one list \bar{y}^j , regarding it as the hypothetical label. This alone is insufficient since other, correctly predicted instances in $\tilde{y}(x, w)$ would lead to a penalization and “over-correcting” gradient $g(x, w, \bar{y}^j)$, given \bar{y}^j as label. This gradient’s optimization goal is, figuratively speaking, to forget to predict everything but \hat{y}^j when presented with x . Note that we cannot simply compute $\nabla_w \mathcal{L}(\hat{y}^j(x, w); \bar{y}^j)$ since regression losses, such as for bounding box regression, are frequently norm-based (e.g., L^p -losses, see Appendix B) such that the respective loss and gradient would both vanish. Therefore, we *secondly* mask \tilde{y} such that the result is likely to only contain output boxes meaning to predict the same instance as \bar{y}^j . Our conditions for this mask are *sufficient score*, *sufficient overlap* with \bar{y}^j and *same in-*

dicated class as \bar{y}^j . We call the subset of \tilde{y} that satisfies these conditions *candidate boxes* for \bar{y}^j , denoted $\text{cand}[\bar{y}^j]$ (for details, refer to Appendix A). We, thus, propose the candidate-restricted self-learning gradient

$$g^{\text{cand}}(x, w, \hat{y}^j) := \nabla_w \mathcal{L}(\text{cand}[\hat{y}^j](x, w), \bar{y}^j) \quad (5)$$

of \hat{y}^j for computing instance-wise uncertainty. This approach is in line with the motivation for the classification setting and extends it when computing (5) for individual contributions to the multi-criterial loss function in object detection (see Appendix B).

Computational complexity. Sampling-based epistemic uncertainty quantification methods such as MC dropout and deep ensembles tend to generate a significant computational overhead as several forward passes are required. Here, we provide a theoretical result on the count of floating point operations (FLOP) of gradient uncertainty metrics which is supported with a proof and additional detail in Appendix D. In our experiments, we use the gradients computed over the last two layers of each network architecture (perhaps of different architectural branches, as well; details in Appendix C). For layer t , we assume stride-1, $(2s_t + 1) \times (2s_t + 1)$ -convolutional layers acting on features maps of spatial size $w_t \times h_t$. These assumptions hold for all architectures in our experiments. We denote the number of input channels by k_{t-1} and of output channels by k_t .

Theorem 1. *The number of FLOP required to compute the last layer ($t = T$) gradient in Eq. (5) is $\mathcal{O}(k_T h w + k_T k_{T-1} (2s_T + 1)^4)$. Similarly, for earlier layers t , we have $\mathcal{O}(k_{t+1} k_t + k_t k_{t-1})$, provided that we have previously computed the gradient for the consecutive layer $t + 1$.*

Performing variational inference only on the last layer requires $\mathcal{O}(k_T k_{T-1} h w)$ FLOP per sample.

Theorem 1 provides that even for MC dropout before the last layer, or the use of efficient deep sub-ensembles [52] sharing the entire architecture but the last layer, gradient metrics require fewer or at worst similar FLOP counts. Earlier sampling, especially entire deep ensembles, have even higher FLOP counts than these variants. Note, however, that computing gradient metrics have somewhat larger computational latency since the full forward pass needs to be computed before the loss gradient can be computed. Moreover, while sampling strategies can in principle be implemented to run all sample forward passes in parallel, the computation of gradients can in principle run in parallel for predicted boxes per image (see Appendix B).

4. Meta classification and meta regression

We evaluate the efficacy of gradient metrics in terms of meta classification and meta regression. These two approaches allow for the *aggregation of potentially large fea-*

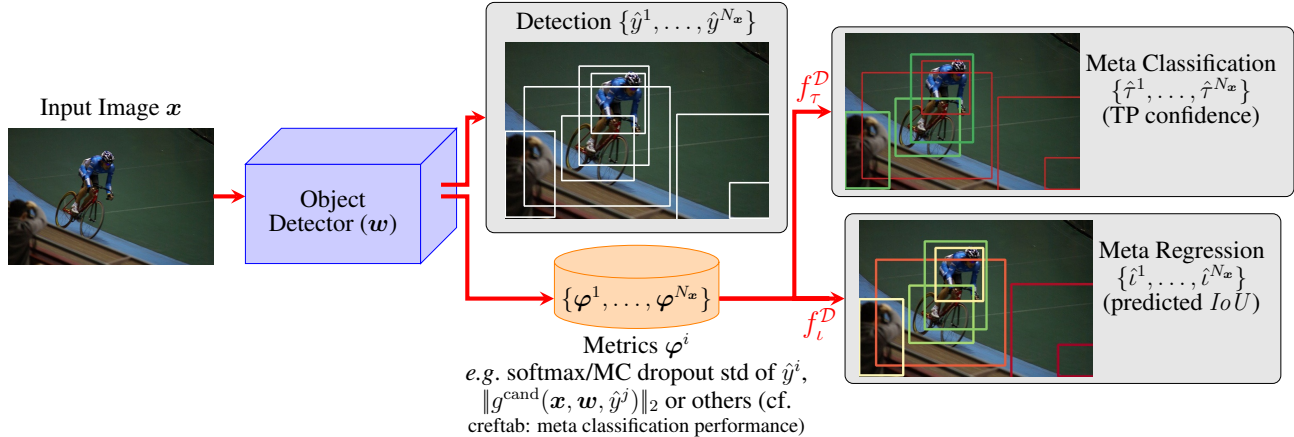


Figure 2. Meta classification and meta regression pipeline: An uncertainty feature vector φ^j is assigned to each detected box \hat{y}^j . During training, we fit f_τ^D and f_i^D to map φ^j to τ^j (TP/FP) and max. IoU i^j of \hat{y}^j , resp. At inference, f_τ^D and f_i^D yield confidence and IoU estimates $\hat{\tau}^j$ and \hat{i}^j for \hat{y}^j based on φ^j .

ture vectors to obtain uncertainty estimates for a respective prediction (e.g., a bounding box). The aim of meta classification is to detect FP predictions by generating confidence estimates while meta regression directly estimates the prediction quality (e.g., IoU). This, in turn, allows for the unified comparison of different uncertainty quantification methods and combinations thereof by regarding meta classifiers and meta regression models based on different features. Moreover, we are able to investigate the degree of mutual redundancy of different sources of uncertainty. In the following, we summarize this method for bounding box detection and illustrate the scheme in Fig. 2.

We regard an object detector generating a list of N_x detections along with a vector φ^j for each predicted bounding box \hat{y}^j . This vector $\varphi^j \in \mathbb{R}^n$ of n “metrics” may contain gradient metrics, but also, e.g., bounding box features, MC dropout or deep ensemble features or combinations thereof (e.g., by concatenation of dropout and ensemble feature vectors). On training data \mathcal{D} , we compute boxes \hat{y} and corresponding metrics $\varphi = (\varphi^1, \dots, \varphi^{N_x})$. We evaluate each predicted instance \hat{y}^j corresponding to the metrics φ^j in terms of their maximal IoU , denoted $i^j \in [0, 1]$ with the respective ground truth and determine FP/TP labels $\tau^j \in \{0, 1\}$ (see Appendix A). A *meta classifier* is a lightweight classification model $f_\tau: \mathbb{R}^n \rightarrow (0, 1)$ giving probabilities for the classification of φ^j (vicariously for the uncertainty of \hat{y}^j) as TP which we fit on \mathcal{D} . Similarly, a *meta regression* model $f_i: \mathbb{R}^n \rightarrow \mathbb{R}$ is fit to the maximum IoU i^j of \hat{y}^j with the ground truth of x . The models f_τ^D and f_i^D can be regarded as post-processing modules which generate confidence measures given an input to an object detector leading to features φ^j . At inference time, we then obtain box-wise classification probabilities $\hat{\tau}^k = f_\tau^D(\varphi^k)$ and IoU predictions $\hat{i}^k = f_i^D(\varphi^k)$. We then determine the

predictive power of f_τ^D and f_i^D in terms of their area under receiver operating characteristic ($AuROC$) or average precision (AP) scores and the coefficient of determination (R^2) scores, respectively.

MetaFusion (object detection post-processing). As a direct application of uncertainty metrics, we investigate an approach inspired by [2]. We implement *meta classification into the object detection pipeline* by assigning each output box in \tilde{y} its meta classification probability as prediction confidence as shown in Fig. 1.

State-of-the-art object detectors use score thresholding in addition to NMS which we compare with confidence filtering based on meta classification. Since for most competitive uncertainty baselines in our experiments, computation for the entire pre-filtering network output \tilde{y} is expensive, we implement a small score threshold which still allows for a large amount of predicted boxes (of ~ 150 bounding boxes per image).

This way, well-performing meta classifiers (which accurately detect FPs) together with an increase in detection sensitivity offer a way to “trade” uncertainty information for detection performance.

Note, that in most object detection pipelines, score thresholding is carried out before NMS. We choose to interchange them here as they commute for the baseline approach. The resulting predictions are compared for a range of confidence thresholds in terms of mean Average Precision (mAP [8]).

5. Experiments

In this section, we report our numerical methods and experimental findings. We investigate meta classification and meta regression on three object detection datasets, namely Pascal VOC [8], MS COCO [27] and KITTI [11]. The

Table 1. Number of layers and losses utilized and resulting numbers of gradient metrics per box. Multiplication in # layers denotes parallel output strands of the resp. DNN (no additional gradients).

Architecture	# layers	# Losses	# gradients
YOLOv3	2×3	3	6
Faster R-CNN	2×4	4	8
RetinaNet	2×2	2	4
Cascade R-CNN	2×8	8	16

splits for training and evaluation we used are given in Appendix C. We investigate for gradient-based meta classification and meta regression for only 2-norm scalars, denoted $GS_{\|\cdot\|_2}$ (refer to Sec. 3), as well as the larger model for all maps listed in Eq. (3), denoted GS_{full} . Gradient metrics are always computed for the last two network layers of each architectural branch and for each contribution to the loss function \mathcal{L} separately, *i.e.*, for classification, bounding box regression and, if applicable, objectness score. We list the resulting counts and number of gradients per investigated architecture in Tab. 1. As meta classifiers and meta regressors, we use gradient boosting models which have been shown [32, 48, 53] to perform well as such. For implementation details, we refer the reader to Appendix C. Whenever we indicate means and standard deviations, we obtained those by 10-fold image-wise cross validation (cv) for the training split \mathcal{D} of the meta classifier / meta regression model. Evaluation is done on the complement of \mathcal{D} .

Comparison with output-based uncertainty. We compare gradient-based uncertainty with various uncertainty baselines in terms of meta classification (Tab. 2) and meta regression (Tab. 3) for a YOLOv3 model with standard Darknet53 backbone [43]. As class probability baselines, we consider objectness score, softmax entropy, energy score [29] and the full softmax distribution per box. Since the full softmax baseline fits a model directly to all class probabilities (as opposed to relying on hand-crafted functions), it can be considered an *enveloping model* to both, entropy and energy score. Moreover, we consider other output baselines in MC dropout (MC), deep ensembles (E) and MetaDetect (MD; details in Appendix C). Since MetaDetect involves the entire network output of a bounding box, it leads to meta classifiers fitted on more variables than class probability baselines. It is, thus, an enveloping model of the full softmax baseline and, therefore, all classification baselines. The results in Tab. 2 indicate that GS_{full} is roughly in the same *AuROC* range as sampling-based uncertainty methods, while being consistently among the two best methods in terms of *AP*. The smaller gradient-based model $GS_{\|\cdot\|_2}$ is consistently better than the full softmax baseline, by up to 3.14 *AuROC* percentage points (ppts) and up to 5.60 *AP* ppts.

We also find that GS_{full} tends to rank lower in terms of *AuROC*. Note also, that MetaDetect is roughly on par with the sampling approaches MC and E throughout. While the latter methods all aim at capturing epistemic uncertainty they constitute approximations and are, thus, not necessarily mutually redundant (cf. crefapp: results).

In addition, we compare the largest sampling and output based model in MC+E+MD and add the gradient metrics GS_{full} to find out about the degree of redundancy between the approximated epistemic uncertainty in MC+E+MD and our method. We note significant boosts to the already well-performing model MC+E+MD across all metrics. Table 3 suggests that gradient uncertainty is especially informative for meta regression with GS_{full} being consistently among the best two models and achieving R^2 scores of up to 85.4 on the KITTI dataset. Adding gradient metrics to MC+E+MD always leads to a gain of more than one R^2 ppt indicating non-redundancy of gradient- and sampling-based metrics.

Object detection architectures. We investigate the applicability and viability of gradient uncertainty for a variety of different architectures. In addition to the YOLOv3 model, we investigate two more standard object detectors in Faster R-CNN [44] and RetinaNet [26] both with a ResNet50 backbone [15]. Moreover, we investigate a stronger object detector in Cascade R-CNN [1] with a large ResNeSt200 [56] backbone which at the time of writing was ranked among the top 10 on the **official COCO Detection Leaderboard**. With a COCO detection *AP* of 49.03, this is in the state-of-the-art range for pure, non-hybrid-task object detectors. In Tab. 4, we list meta classification *AuROC* and meta regression R^2 for the score, MetaDetect (representing output-based methods), GS_{full} and the combined model GS_{full} +MD. We see GS_{full} again being on par with MD, in the majority of cases even surpassing it by up to 2.01 *AuROC* ppts and up to 11.52 R^2 ppts. When added to MD, we find again boosts in both performance metrics, especially in R^2 . On the COCO dataset, the high performance model Cascade R-CNN delivers a remarkably strong Score baseline completely redundant with MD and surpassing GS_{full} on its own. However, here we also find an improvement of 0.68 ppts by adding gradient information.

Calibration. We evaluate the meta classifier confidences obtained above in terms of their calibration errors when divided into 10 confidence bins. Exemplary reliability plots are shown in Fig. 3 for the Score, MD and GS_{full} together with corresponding expected (*ECE* [38]) and average (*ACE* [39]) calibration errors. The Score is clearly over-confident in the upper confidence range and both meta classifiers are well-calibrated. Both calibration errors of the latter are about one order of magnitude smaller than those of the score. We show the full table of calibration errors

Table 2. Meta classification performance in terms of $AuROC$ and AP per confidence model over 10-fold cv (mean \pm std).

YOLOv3	Pascal VOC		COCO		KITTI	
	$AuROC$	AP	$AuROC$	AP	$AuROC$	AP
Score	90.68 \pm 0.06	69.56 \pm 0.12	82.97 \pm 0.04	62.31 \pm 0.05	96.53 \pm 0.05	96.87 \pm 0.03
Entropy	91.30 \pm 0.02	61.94 \pm 0.06	76.52 \pm 0.02	42.52 \pm 0.04	94.79 \pm 0.06	94.83 \pm 0.05
Energy Score [29]	92.59 \pm 0.02	64.65 \pm 0.06	75.39 \pm 0.02	39.72 \pm 0.06	95.66 \pm 0.02	95.33 \pm 0.03
Full Softmax	93.81 \pm 0.06	72.08 \pm 0.15	82.91 \pm 0.06	58.65 \pm 0.10	97.07 \pm 0.03	96.85 \pm 0.03
MC Dropout [50] (MC)	96.72 \pm 0.02	78.15 \pm 0.09	89.04 \pm 0.02	64.94 \pm 0.11	97.60 \pm 0.07	97.17 \pm 0.10
Ensemble [25] (E)	96.87 \pm 0.02	77.86 \pm 0.11	88.97 \pm 0.02	64.05 \pm 0.12	97.63 \pm 0.04	97.63 \pm 0.05
MetaDetect [48] (MD)	95.78 \pm 0.05	78.64 \pm 0.08	87.16 \pm 0.04	<u>69.41 \pm 0.07</u>	98.23 \pm 0.02	98.06 \pm 0.02
Grad. Score $_{\parallel-\parallel_2}$ (GS $_{\parallel-\parallel_2}$; ours)	94.76 \pm 0.03	74.86 \pm 0.10	86.05 \pm 0.04	64.25 \pm 0.06	97.31 \pm 0.05	96.86 \pm 0.10
Grad. Score $_{full}$ (GS $_{full}$; ours)	95.80 \pm 0.04	<u>78.57 \pm 0.11</u>	88.07 \pm 0.03	69.62 \pm 0.07	<u>98.04 \pm 0.03</u>	<u>97.81 \pm 0.06</u>
MC+E+MD (ours)	97.66 \pm 0.02	85.13 \pm 0.12	91.14 \pm 0.02	73.82 \pm 0.05	98.56 \pm 0.03	98.45 \pm 0.03
GS $_{full}$ +MC+E+MD (ours)	97.95 \pm 0.02	86.69 \pm 0.09	91.65 \pm 0.03	74.88 \pm 0.07	98.74 \pm 0.02	98.62 \pm 0.01

Table 3. Meta regression performance in terms of R^2 per confidence model over 10-fold cv (mean \pm std).

YOLOv3	Pascal VOC	COCO	KITTI
Score	48.29 \pm 0.04	32.60 \pm 0.02	78.86 \pm 0.05
Entropy	43.24 \pm 0.03	21.10 \pm 0.04	69.33 \pm 0.04
Energy Score	47.18 \pm 0.03	17.94 \pm 0.02	71.53 \pm 0.10
Full Softmax	53.86 \pm 0.11	36.95 \pm 0.13	78.92 \pm 0.11
MC	<u>61.63 \pm 0.15</u>	43.85 \pm 0.09	82.10 \pm 0.11
E	61.48 \pm 0.07	43.53 \pm 0.13	84.18 \pm 0.12
MD	60.36 \pm 0.14	<u>44.22 \pm 0.11</u>	85.88 \pm 0.10
GS $_{\parallel-\parallel_2}$ (ours)	58.05 \pm 0.13	38.77 \pm 0.04	81.21 \pm 0.05
GS $_{full}$ (ours)	62.50 \pm 0.11	44.90 \pm 0.09	<u>85.40 \pm 0.11</u>
MC+E+MD	69.38 \pm 0.11	54.07 \pm 0.08	87.78 \pm 0.11
GS $_{full}$ +MC+E+MD	72.26 \pm 0.08	56.14 \pm 0.11	88.80 \pm 0.07

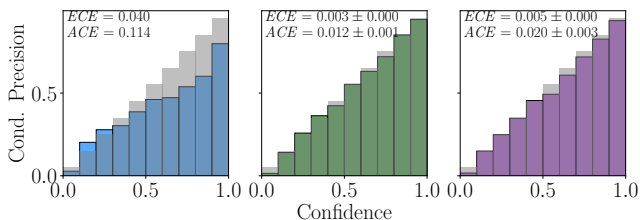


Figure 3. Reliability plots of the Score (left) and meta classifiers for MD (center) and GS $_{full}$ (right) on the Pascal VOC dataset for YOLOv3 with calibration errors (mean \pm std).

including maximum calibration error in Appendix E.

Pedestrian detection. The statistical improvement seen in meta classification performance may not hold for non-majority classes within a dataset which are regularly safety-relevant. We investigate meta classification of the “Pedestrian” class in KITTI and explicitly study the FP/FN trade-off. This can be accomplished by sweeping the confidence threshold between 0 and 1 and counting the resulting FPs and FNs. We choose increments of 10^{-2} for meta classifiers and 10^{-4} for the scores as to not interpolate too roughly in the range of very small score values where a significant number of predictions cluster. The resulting curves

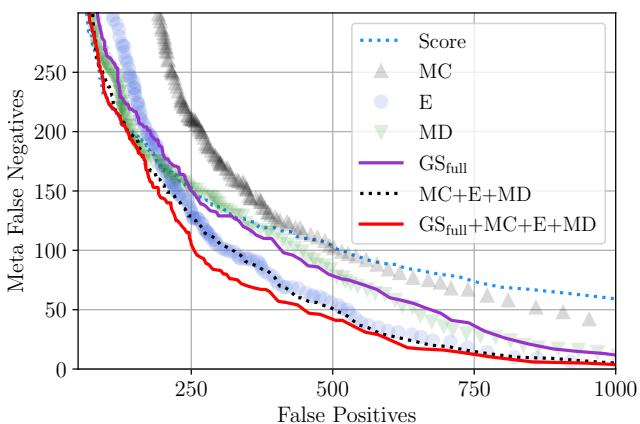


Figure 4. Meta classification for the class “Pedestrian”. Curves obtained by sweeping the threshold on score / meta classification probability. Note the FP gaps for ≤ 100 FNs.

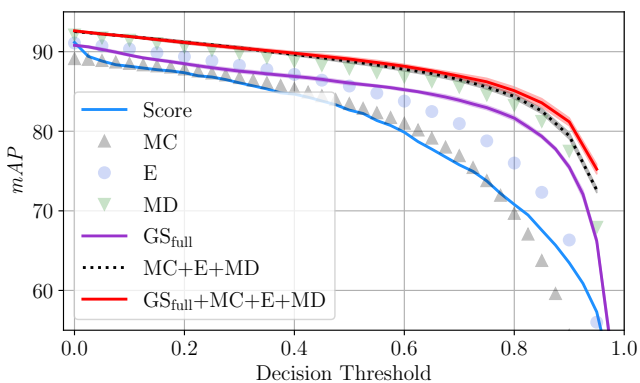


Figure 5. Score baseline and MetaFusion mAP . Error bands we draw around meta classifiers indicate cv-std.

are depicted in Fig. 4. For applications in safety-critical environments, not all errors need to be equally important. We may, for example, demand a good trade-off at a given

Table 4. Meta classification and meta regression performance in terms of $AuROC$ and R^2 , respectively, for different object detection architectures. Results (mean \pm std) obtained from 10-fold cv as above.

	Pascal VOC		COCO		KITTI	
	$AuROC$	R^2	$AuROC$	R^2	$AuROC$	R^2
Faster R-CNN						
Score	89.77 \pm 0.05	39.94 \pm 0.02	83.82 \pm 0.03	40.50 \pm 0.01	96.53 \pm 0.05	72.29 \pm 0.02
MD	94.43 \pm 0.02	47.92 \pm 0.09	91.31 \pm 0.02	44.41 \pm 0.04	98.86 \pm 0.02	79.92 \pm 0.04
GS _{full}	95.88 \pm 0.05	59.40 \pm 0.03	91.38 \pm 0.03	50.44 \pm 0.04	99.20 \pm 0.01	86.31 \pm 0.07
GS _{full} + MD	96.77 \pm 0.05	63.64 \pm 0.08	92.30 \pm 0.02	52.30 \pm 0.04	99.37 \pm 0.02	87.46 \pm 0.05
RetinaNet						
Score	87.53 \pm 0.03	40.43 \pm 0.01	84.95 \pm 0.02	39.88 \pm 0.02	95.91 \pm 0.02	73.44 \pm 0.02
MD	89.57 \pm 0.04	50.27 \pm 0.10	85.09 \pm 0.01	42.45 \pm 0.12	96.19 \pm 0.02	77.53 \pm 0.08
GS _{full}	91.58 \pm 0.04	57.23 \pm 0.07	85.59 \pm 0.02	47.74 \pm 0.06	97.26 \pm 0.03	84.47 \pm 0.04
GS _{full} + MD	92.99 \pm 0.03	64.32 \pm 0.07	87.15 \pm 0.05	51.07 \pm 0.09	97.61 \pm 0.02	85.73 \pm 0.09
Cascade R-CNN						
Score	95.70 \pm 0.04	57.90 \pm 0.09	94.11 \pm 0.01	56.31 \pm 0.01	98.67 \pm 0.02	83.31 \pm 0.03
MD	96.32 \pm 0.05	63.62 \pm 0.12	94.10 \pm 0.02	58.74 \pm 0.08	99.18 \pm 0.01	86.22 \pm 0.08
GS _{full}	96.66 \pm 0.05	63.94 \pm 0.13	93.97 \pm 0.01	57.80 \pm 0.08	99.34 \pm 0.01	87.39 \pm 0.08
GS _{full} + MD	97.24 \pm 0.05	69.78 \pm 0.13	94.78 \pm 0.02	62.13 \pm 0.06	99.48 \pm 0.01	89.59 \pm 0.04

FN count which is usually desired to be especially small. Our present evaluation split contains a total of 1152 pedestrian instances. Assume that we allowed for a detector to miss around 100 pedestrians ($\sim 10\%$), we see a reduction in FPs for some meta classifiers. MD and GS_{full} are very roughly on par, leading to a reduction of close to 100 FPs. The ensemble E turns out to be about as effective as the entire output-based model MC+E+MD, only falling behind above 150 FNs. This indicates a certain degree of redundancy between output-based methods. Adding GS_{full} to MC+E+MD, however, reduces the number of FPs again by about 100 leading to an FP difference of about 250 as compared to the Score baseline. Observing the trend, the improvements become even more effective for smaller numbers of FNs (small thresholds) but diminish for larger numbers of above 200 FNs.

MetaFusion.

In regarding Fig. 2, meta classifiers naturally fit as post processing modules on top of object detection pipelines. Doing so does not generate new bounding boxes, but modifies the confidence ranking as shown in Fig. 1 and may also lead to calibrated confidences. Therefore, the score baseline and meta classifiers are not comparable for fixed decision thresholds. We obtain a comparison of the resulting object detection performance by sweeping the decision threshold with a step size of 0.05 (resp. 0.025 for Score). The mAP curves are shown in Fig. 5. We draw error bands showing cv-std for GS_{full}, MC+E+MD and GS_{full}+MC+E+MD. Meta classification-based decision rules are either on par (MC) with the score threshold or consistently allow for an mAP improvement of at least 1 to 2 mAP ppts. In particular, MD performs well, gaining around 2 ppts in the max-

imum mAP . When comparing the addition of GS_{full} to MC+E+MD, we still find slim improvements for thresholds ≥ 0.75 . The score curve shows a kink at a threshold of 0.05 and ends at the same maximum mAP as GS_{full} while the confidence ranking is clearly improved for MC+E+MD and GS_{full}+MC+E+MD. Note that meta classification based on GS_{full} is less sensitive to the choice of threshold than the score in the medium range. At a threshold of 0.3 we have an mAP gap of about 1.4 ppts which widens to 5.2 ppts at 0.6.

6. Conclusion

Applications of modern DNNs in safety-critical environments demand high performance on the one hand, but also reliable confidence estimation indicating where a model is not competent.

Novel uncertainty quantification methods tend to be developed in the simplified classification setting, the transfer of which to instance-based recognition tasks entails conceptual complications. We have proposed and investigated a way of implementing gradient-based uncertainty quantification for deep object detection which complements output-based methods well and is on par with established epistemic uncertainty metrics. Experiments involving a number of different architectures suggest that our method can be applied to significant benefit across architectures, even for high performance state-of-the-art models. We showed that meta classification performance carries over to object detection performance when employed as a post-processing module and that meta classification naturally leads to well-calibrated gradient confidences which improves probabilis-

tic reliability. Our trade-off study indicates that gradient uncertainty reduces the FP/FN ratio for non-majority classes, especially when paired with output-based methods which, however, considerably increases computational overhead.

While our experiments indicate the viability of gradient-based uncertainty for deep object detection empirically, we believe that a well-founded theoretical justification would further greatly benefit and advance the research area. Also, a comparison of gradient metrics in terms of OoD (or “open set condition”) detections would be of great service and in line with previous work on gradient uncertainty [17, 40, 53]. However, the very definition of OoD in the instance-based setting is still subject of contemporary research itself [6, 19, 36] and lacks a widely established definition.

Equation (5) can in principle be augmented to fit any DNN inferring and learning on an instance-based logic such as 3D bounding box detection or instance segmentation. Further applications of our method may include uncertainty-based querying in active learning or the probabilistic detection of data annotation errors. We hope that this work will inspire future progress in uncertainty quantification, probabilistic object detection and related areas.

Foreseeable impact. While we see great benefits in increasing the safety of human lives through improved confidence estimation, we also note that the usage of machine learning models in confidence calibration based on gradient information adds another failure mode, which, if applied in automated driving, could lead to fatal consequences, if false predictions of confidence occur. It is, therefore, necessary to be aware of the low technology readiness level of the method introduced here. Despite the evidence provided that our method can significantly reduce the number of false negative pedestrians of an object detector for certain datasets, application of our method in a safety-critical context requires extensive testing to demonstrate robustness, e.g., with respect to domain shifts, prior to any integration into applications.

Technical Limitations. We have argued that while sampling-based uncertainty quantification methods can be run in parallel across models, gradients can be computed in parallel across predicted bounding boxes.

Nevertheless, we emphasize that the usage of gradient uncertainty metrics introduces a factor of computational latency in that metrics can be computed only after the prediction. Sampling-based methods do not suffer from this mechanism which should be considered, e.g. for real-time applications.

Acknowledgement. The research leading to these results is funded by the German Federal Ministry for Economic Affairs and Energy within the project “Methoden und Maßnahmen zur Absicherung von KI basierten

Wahrnehmungsfunktionen für das automatisierte Fahren (KI-Absicherung)”. The authors would like to thank the consortium for the successful cooperation. Furthermore, we gratefully acknowledge financial support by the state Ministry of Economy, Innovation and Energy of Northrhine Westphalia (MWIDE) and the European Fund for Regional Development via the FIS.NRW project BIT-KI, grant no. EFRE-0400216. The authors gratefully acknowledge the Gauss Centre for Supercomputing e.V. (www.gauss-centre.eu) for funding this project by providing computing time through the John von Neumann Institute for Computing (NIC) on the GCS Supercomputer JUWELS at Jülich Supercomputing Centre (JSC).

References

- [1] Zhaowei Cai and Nuno Vasconcelos. Cascade r-cnn: Delving into high quality object detection. In *Proceedings of the IEEE conference on computer vision and pattern recognition*, pages 6154–6162, 2018. 1, 6, 14, 16
- [2] Robin Chan, Matthias Rottmann, Fabian Hüger, Peter Schlicht, and Hanno Gottschalk. Metafusion: Controlled false-negative reduction of minority classes in semantic segmentation. *arXiv preprint arXiv:1912.07420*, 2019. 3, 5
- [3] Tianqi Chen and Carlos Guestrin. XGBoost: A scalable tree boosting system. In *Proceedings of the 22nd ACM SIGKDD International Conference on Knowledge Discovery and Data Mining, KDD '16*, pages 785–794, New York, NY, USA, 2016. ACM. 19, 21
- [4] Charles Corbière, Nicolas Thome, Avner Bar-Hen, Matthieu Cord, and Patrick Pérez. Addressing failure prediction by learning model confidence. In *33rd Conference on Neural Information Processing Systems (NeurIPS 2019)*, pages 2898–2909. Curran Associates, Inc., 2019. 2, 3
- [5] John S Denker and Yann LeCun. Transforming neural-net output levels to probability distributions. In *Proceedings of the 3rd International Conference on Neural Information Processing Systems*, pages 853–859, 1990. 2
- [6] Akshay Dharmija, Manuel Gunther, Jonathan Ventura, and Terrance Boulton. The overlooked elephant of object detection: Open set. In *Proceedings of the IEEE/CVF Winter Conference on Applications of Computer Vision*, pages 1021–1030, 2020. 9
- [7] John Duchi, Elad Hazan, and Yoram Singer. Adaptive sub-gradient methods for online learning and stochastic optimization. *Journal of machine learning research*, 12(7), 2011. 12
- [8] M. Everingham, L. Van Gool, C. K. I. Williams, J. Winn, and A. Zisserman. The pascal visual object classes (voc) challenge. *International Journal of Computer Vision*, 88(2):303–338, June 2010. 5, 16
- [9] Yarin Gal. *Uncertainty in deep learning*. PhD thesis, University of Cambridge, 2016. 2
- [10] Yarin Gal and Zoubin Ghahramani. Dropout as a bayesian approximation: Representing model uncertainty in deep

- learning. In *international conference on machine learning*, pages 1050–1059. PMLR, 2016. 2
- [11] Andreas Geiger, P Lenz, Christoph Stiller, and Raquel Urtasun. The kitti vision benchmark suite. URL <http://www.cvlibs.net/datasets/kitti>, 2, 2015. 5, 16
- [12] Ian J Goodfellow, Jonathon Shlens, and Christian Szegedy. Explaining and harnessing adversarial examples. *arXiv preprint arXiv:1412.6572*, 2014. 2
- [13] Chuan Guo, Geoff Pleiss, Yu Sun, and Kilian Q Weinberger. On calibration of modern neural networks. In *International Conference on Machine Learning*, pages 1321–1330. PMLR, 2017. 2
- [14] Ali Harakeh, Michael Smart, and Steven L Waslander. Bayesod: A bayesian approach for uncertainty estimation in deep object detectors. In *2020 IEEE International Conference on Robotics and Automation (ICRA)*, pages 87–93. IEEE, 2020. 2
- [15] Kaiming He, Xiangyu Zhang, Shaoqing Ren, and Jian Sun. Deep residual learning for image recognition. In *Proceedings of the IEEE conference on computer vision and pattern recognition*, pages 770–778, 2016. 6, 16
- [16] Dan Hendrycks and Kevin Gimpel. A baseline for detecting misclassified and out-of-distribution examples in neural networks. *arXiv preprint arXiv:1610.02136*, 2016. 3
- [17] Rui Huang, Andrew Geng, and Yixuan Li. On the importance of gradients for detecting distributional shifts in the wild. *Advances in Neural Information Processing Systems*, 34, 2021. 2, 9
- [18] Eyke Hüllermeier and Willem Waegeman. Aleatoric and epistemic uncertainty in machine learning: An introduction to concepts and methods. *Machine Learning*, pages 1–50, 2021. 2
- [19] KJ Joseph, Salman Khan, Fahad Shahbaz Khan, and Vineeth N Balasubramanian. Towards open world object detection. In *Proceedings of the IEEE/CVF Conference on Computer Vision and Pattern Recognition*, pages 5830–5840, 2021. 9
- [20] Alex Kendall and Yarin Gal. What uncertainties do we need in bayesian deep learning for computer vision? In I. Guyon, U. V. Luxburg, S. Bengio, H. Wallach, R. Fergus, S. Vishwanathan, and R. Garnett, editors, *Advances in Neural Information Processing Systems*, volume 30. Curran Associates, Inc., 2017. 2
- [21] Diederik P Kingma and Jimmy Ba. Adam: A method for stochastic optimization. *arXiv preprint arXiv:1412.6980*, 2014. 12
- [22] Kamil Kowol., Matthias Rottmann., Stefan Bracke., and Hanno Gottschalk. Yodar: Uncertainty-based sensor fusion for vehicle detection with camera and radar sensors. In *Proceedings of the 13th International Conference on Agents and Artificial Intelligence - Volume 2: ICAART.*, pages 177–186. INSTICC, SciTePress, 2021. 3
- [23] Florian Kraus and Klaus Dietmayer. Uncertainty estimation in one-stage object detection. In *2019 IEEE Intelligent Transportation Systems Conference (ITSC)*, pages 53–60. IEEE, 2019. 3
- [24] Fabian Kuppers, Jan Kronenberger, Amirhossein Shantia, and Anselm Haselhoff. Multivariate confidence calibration for object detection. In *Proceedings of the IEEE/CVF Conference on Computer Vision and Pattern Recognition Workshops*, pages 326–327, 2020. 13
- [25] Balaji Lakshminarayanan, Alexander Pritzel, and Charles Blundell. Simple and scalable predictive uncertainty estimation using deep ensembles. In *Proceedings of the 31st International Conference on Neural Information Processing Systems, NIPS’17*, page 6405–6416, Red Hook, NY, USA, 2017. Curran Associates Inc. 2, 7
- [26] Tsung-Yi Lin, Priya Goyal, Ross Girshick, Kaiming He, and Piotr Dollár. Focal loss for dense object detection. In *Proceedings of the IEEE international conference on computer vision*, pages 2980–2988, 2017. 1, 6, 12, 15, 16
- [27] Tsung-Yi Lin, Michael Maire, Serge Belongie, James Hays, Pietro Perona, Deva Ramanan, Piotr Dollár, and C Lawrence Zitnick. Microsoft coco: Common objects in context. In *European conference on computer vision*, pages 740–755. Springer, 2014. 5, 16
- [28] Wei Liu, Dragomir Anguelov, Dumitru Erhan, Christian Szegedy, Scott Reed, Cheng-Yang Fu, and Alexander C Berg. Ssd: Single shot multibox detector. In *European conference on computer vision*, pages 21–37. Springer, 2016. 1
- [29] Weitang Liu, Xiaoyun Wang, John Owens, and Yixuan Li. Energy-based out-of-distribution detection. *Advances in Neural Information Processing Systems*, 33, 2020. 3, 6, 7, 17
- [30] Zongyao Lyu, Nolan Gutierrez, Aditya Rajguru, and William J Beksi. Probabilistic object detection via deep ensembles. In *European Conference on Computer Vision*, pages 67–75. Springer, 2020. 2, 3
- [31] Kira Maag, Matthias Rottmann, and Hanno Gottschalk. Time-dynamic estimates of the reliability of deep semantic segmentation networks. In *2020 IEEE 32nd International Conference on Tools with Artificial Intelligence (IC-TAI)*, pages 502–509. IEEE, 2020. 3
- [32] Kira Maag, Matthias Rottmann, Fabian Hüger, Peter Schlicht, and Hanno Gottschalk. Improving video instance segmentation by light-weight temporal uncertainty estimates. *arXiv preprint arXiv:2012.07504*, 2020. 3, 6
- [33] David JC MacKay. A practical bayesian framework for back-propagation networks. *Neural computation*, 4(3):448–472, 1992. 2
- [34] Andrey Malinin and Mark Gales. Predictive uncertainty estimation via prior networks. In *Proceedings of the 32nd International Conference on Neural Information Processing Systems*, pages 7047–7058, 2018. 2
- [35] Dimity Miller, Feras Dayoub, Michael Milford, and Niko Sünderhauf. Evaluating merging strategies for sampling-

- based uncertainty techniques in object detection. In *2019 International Conference on Robotics and Automation (ICRA)*, pages 2348–2354, 2019. [2](#), [3](#)
- [36] Dimity Miller, Lachlan Nicholson, Feras Dayoub, and Niko Sünderhauf. Dropout sampling for robust object detection in open-set conditions. In *2018 IEEE International Conference on Robotics and Automation (ICRA)*, pages 3243–3249. IEEE, 2018. [2](#), [3](#), [9](#)
- [37] Dimity Miller, Niko Sünderhauf, Haoyang Zhang, David Hall, and Feras Dayoub. Benchmarking sampling-based probabilistic object detectors. In *CVPR Workshops*, volume 3, page 6, 2019. [2](#), [3](#)
- [38] Mahdi Pakdaman Naeni, Gregory Cooper, and Milos Hauskrecht. Obtaining well calibrated probabilities using bayesian binning. In *Proceedings of the AAAI Conference on Artificial Intelligence*, volume 29, 2015. [6](#), [13](#), [14](#), [24](#)
- [39] Lukas Neumann, Andrew Zisserman, and Andrea Vedaldi. Relaxed softmax: Efficient confidence auto-calibration for safe pedestrian detection. In *NIPS 2018 Workshop MLITS*, 2018. [6](#), [13](#), [14](#), [24](#)
- [40] Philipp Oberdiek, Matthias Rottmann, and Hanno Gottschalk. Classification uncertainty of deep neural networks based on gradient information. In *IAPR Workshop on Artificial Neural Networks in Pattern Recognition*, pages 113–125. Springer, 2018. [2](#), [3](#), [9](#), [17](#), [18](#)
- [41] Adam Paszke, Sam Gross, Francisco Massa, Adam Lerer, James Bradbury, Gregory Chanan, Trevor Killeen, Zeming Lin, Natalia Gimelshein, Luca Antiga, Alban Desmaison, Andreas Kopf, Edward Yang, Zachary DeVito, Martin Raison, Alykhan Tejani, Sasank Chilamkurthy, Benoit Steiner, Lu Fang, Junjie Bai, and Soumith Chintala. Pytorch: An imperative style, high-performance deep learning library. In H. Wallach, H. Larochelle, A. Beygelzimer, F. d’Alché-Buc, E. Fox, and R. Garnett, editors, *Advances in Neural Information Processing Systems 32*, pages 8024–8035. Curran Associates, Inc., 2019. [16](#)
- [42] Tiago Ramalho and Miguel Miranda. Density estimation in representation space to predict model uncertainty. In *International Workshop on Engineering Dependable and Secure Machine Learning Systems*, pages 84–96. Springer, 2020. [2](#)
- [43] Joseph Redmon and Ali Farhadi. Yolov3: An incremental improvement. *arXiv preprint arXiv:1804.02767*, 2018. [1](#), [6](#), [12](#), [14](#), [16](#)
- [44] Shaoqing Ren, Kaiming He, Ross Girshick, and Jian Sun. Faster r-cnn: Towards real-time object detection with region proposal networks. In C. Cortes, N. Lawrence, D. Lee, M. Sugiyama, and R. Garnett, editors, *Advances in Neural Information Processing Systems*, volume 28. Curran Associates, Inc., 2015. [1](#), [6](#), [12](#), [14](#), [16](#)
- [45] Matthias Rottmann, Pascal Colling, Thomas Paul Hack, Robin Chan, Fabian Hüger, Peter Schlicht, and Hanno Gottschalk. Prediction error meta classification in semantic segmentation: Detection via aggregated dispersion measures of softmax probabilities. In *2020 International Joint Conference on Neural Networks (IJCNN)*, pages 1–9. IEEE, 2020. [3](#)
- [46] Matthias Rottmann, Kira Maag, Robin Chan, Fabian Hüger, Peter Schlicht, and Hanno Gottschalk. Detection of false positive and false negative samples in semantic segmentation. In *Proceedings of the 23rd Conference on Design, Automation and Test in Europe, DATE ’20*, page 1351–1356, San Jose, CA, USA, 2020. EDA Consortium. [3](#)
- [47] Matthias Rottmann and Marius Schubert. Uncertainty measures and prediction quality rating for the semantic segmentation of nested multi resolution street scene images. In *Proceedings of the IEEE/CVF Conference on Computer Vision and Pattern Recognition Workshops*, 2019. [3](#)
- [48] Marius Schubert, Karsten Kahl, and Matthias Rottmann. Metadetect: Uncertainty quantification and prediction quality estimates for object detection. *arXiv preprint arXiv:2010.01695*, 2020. [2](#), [3](#), [6](#), [7](#), [18](#)
- [49] Shai Shalev-Shwartz and Shai Ben-David. *Understanding machine learning: From theory to algorithms*. Cambridge university press, 2014. [19](#)
- [50] Nitish Srivastava, Geoffrey Hinton, Alex Krizhevsky, Ilya Sutskever, and Ruslan Salakhutdinov. Dropout: a simple way to prevent neural networks from overfitting. *The journal of machine learning research*, 15(1):1929–1958, 2014. [2](#), [7](#)
- [51] Christian Szegedy, Wojciech Zaremba, Ilya Sutskever, Joan Bruna, Dumitru Erhan, Ian Goodfellow, and Rob Fergus. Intriguing properties of neural networks. *arXiv preprint arXiv:1312.6199*, 2013. [2](#)
- [52] Matias Valdenegro-Toro. Deep sub-ensembles for fast uncertainty estimation in image classification. *4th workshop on Bayesian Deep Learning (NeurIPS 2019)*, 2019. [4](#), [21](#)
- [53] Vishal Thanvantri Vasudevan, Abhinav Sethy, and Alireza Roshan Ghias. Towards better confidence estimation for neural models. In *ICASSP 2019-2019 IEEE International Conference on Acoustics, Speech and Signal Processing (ICASSP)*, pages 7335–7339. IEEE, 2019. [2](#), [3](#), [6](#), [9](#)
- [54] Haoyu Wu. Yolov3-in-pytorch. <https://github.com/westerndigitalcorporation/YOLOv3-in-PyTorch>, 2018. [16](#)
- [55] Yuxin Wu, Alexander Kirillov, Francisco Massa, Wan-Yen Lo, and Ross Girshick. Detectron2. <https://github.com/facebookresearch/detectron2>, 2019. [17](#)
- [56] Hang Zhang, Chongruo Wu, Zhongyue Zhang, Yi Zhu, Zhi Zhang, Haibin Lin, Yue Sun, Tong He, Jonas Muller, R. Manmatha, Mu Li, and Alexander Smola. Resnest: Split-attention networks. *arXiv preprint arXiv:2004.08955*, 2020. [6](#), [16](#), [17](#)

A. Object Detection

A.1. Notation.

We regard the task of 2D bounding box detection on camera images. Here, the detection

$$\hat{y}(\mathbf{x}, \mathbf{w}) = (\hat{y}^1(\mathbf{x}, \mathbf{w}), \dots, \hat{y}^{N_x}(\mathbf{x}, \mathbf{w})) \in \mathbb{R}^{N_x \times (4+1+C)} \quad (6)$$

on an input image \mathbf{x} , depending on model weights \mathbf{w} , consists of a number $N_x \in \mathbb{N}$ (dependent on the input \mathbf{x}) of instances \hat{y}^j . We give a short account of its constituents. Each instance

$$\hat{y}^j = (\hat{\xi}^j, \hat{s}^j, \hat{p}^j) \in \mathbb{R}^{4+1+C} \quad (7)$$

consists of localizations $\hat{\xi}^j = (\hat{x}^j, \hat{y}^j, \hat{w}^j, \hat{h}^j)$ encoded e.g. as center coordinates \hat{x}, \hat{y} together with width \hat{w} and height \hat{h} . Moreover, a list of N_x integers $\hat{\kappa} \in \{1, \dots, C\}$ represents the predicted categories for the object found in the respective boxes out of a pre-determined fixed list of $C \in \mathbb{N}$ possible categories. Usually, $\hat{\kappa}$ is obtained as the arg max of a learnt probability distribution $\hat{p} = (\hat{p}_1, \dots, \hat{p}_C) \in (0, 1)^C$ over all C categories. Finally, N_x scores $\hat{s} \in (0, 1)$ indicate the probability of each box being correct.

The predicted N_x boxes are obtained by different filtering mechanisms as a subset of a fixed number N_{out} (usually about 10^5 to 10^6) of output boxes

$$\tilde{y}(\mathbf{x}, \mathbf{w}) = (\tilde{y}^1, \dots, \tilde{y}^{N_{\text{out}}}). \quad (8)$$

The latter are the regression and classification result of pre-determined ‘‘prior’’ or ‘‘anchor boxes’’. Predicted box localization $\hat{\xi}$ is usually learned as offsets and width- and height scaling of fixed anchor boxes [26, 43] or region proposals [44] (see Appendix B). The most prominent examples (and the ones employed in all architectures we investigate) of filtering mechanisms are *score thresholding* and *Non-Maximum Suppression*. By score thresholding we mean only allowing boxes which have $\hat{s} \geq \varepsilon_s$ for some fixed threshold $\varepsilon_s \geq 0$.

A.2. Non-Maximum Suppression (NMS).

NMS is an algorithm allowing for different output boxes that have the same class and significant mutual overlap (meaning they are likely to indicate the same visible instance in \mathbf{x}) to be reduced to only one box. Overlap is usually quantified as *intersection over union (IoU)*. For two bounding boxes A and B , their intersection over union is

$$IoU(A, B) = \frac{|A \cap B|}{|A \cup B|}, \quad (9)$$

i.e., the ratio of the area of intersection of two boxes and the joint area of those two boxes, where 0 means no overlap and

1 means the boxes have identical location and size. Maximal mutual *IoU* between a predicted box \hat{y}^j and ground truth boxes y is also used to quantify the quality of the prediction of a given instance.

We call an output instance \hat{y}^i ‘‘candidate box’’ for another box \hat{y}^j if it fulfills the following requirements:

1. score ($\hat{s}^i \geq \varepsilon_s$ above a chosen, fixed threshold ε_s)
2. identical class $\hat{\kappa}^i = \hat{\kappa}^j$
3. large mutual overlap $IoU(\hat{y}^i, \hat{y}^j) \geq \varepsilon_{IoU}$ for some fixed threshold $\varepsilon_{IoU} \geq 0$ (a widely accepted choice which we adopt is $\varepsilon_{IoU} = 0.5$).

We denote the set of output candidate boxes for \hat{y}^j by $\text{cand}[\hat{y}^j]$. Note, that we can also determine candidate boxes for an output box \tilde{y}^j . In NMS, all output boxes are sorted by their score in descending order. Then, the box with the best score is selected as a prediction and all candidates for that box are deleted from the ranked list. This is done until there are no boxes with $\hat{s} \geq \varepsilon_s$ left. Thereby selected boxes form the N_x predictions.

A.3. Training of object detectors.

The ‘‘ground truth’’ or ‘‘label’’ data y from which an object detector learns must contain localization information ξ^j for each of $j = 1, \dots, N_x$ annotated instances on each data point \mathbf{x} , as well as the associated N_x category indices κ^j . Note that we denote labels by the same symbol as the corresponding predicted quantity and omit the hat ($\hat{\cdot}$).

Generically, deep object detectors are trained by stochastic gradient descent or some variant such as AdaGrad [7], or Adam [21] by minimizing an empirical loss

$$\mathcal{L} = \mathcal{L}_\xi + \mathcal{L}_s + \mathcal{L}_p. \quad (10)$$

For all object detection frameworks which we consider here (and most architectures, in general) the loss function \mathcal{L} splits up additively into parts punishing localization inaccuracies ($\tilde{\xi}$), score (\tilde{s}) assignment to boxes (assigning large loss to high score for incorrect boxes and low score for correct boxes) and incorrect class probability distribution (\tilde{p}), respectively. We explicitly give formulas for all utilized loss functions in Appendix B. The trainable weights \mathbf{w} of the model are updated in standard gradient descent optimization by

$$\mathbf{w} \leftarrow \mathbf{w} - \eta \nabla_{\mathbf{w}} \mathcal{L}(\tilde{y}(\mathbf{x}, \mathbf{w}), y) \quad (11)$$

where η is a learning rate factor. We denote by $g(\mathbf{x}, \mathbf{w}, y) := \nabla_{\mathbf{w}} \mathcal{L}(\tilde{y}(\mathbf{x}, \mathbf{w}); y)$ the learning gradient on the data point (\mathbf{x}, y) .

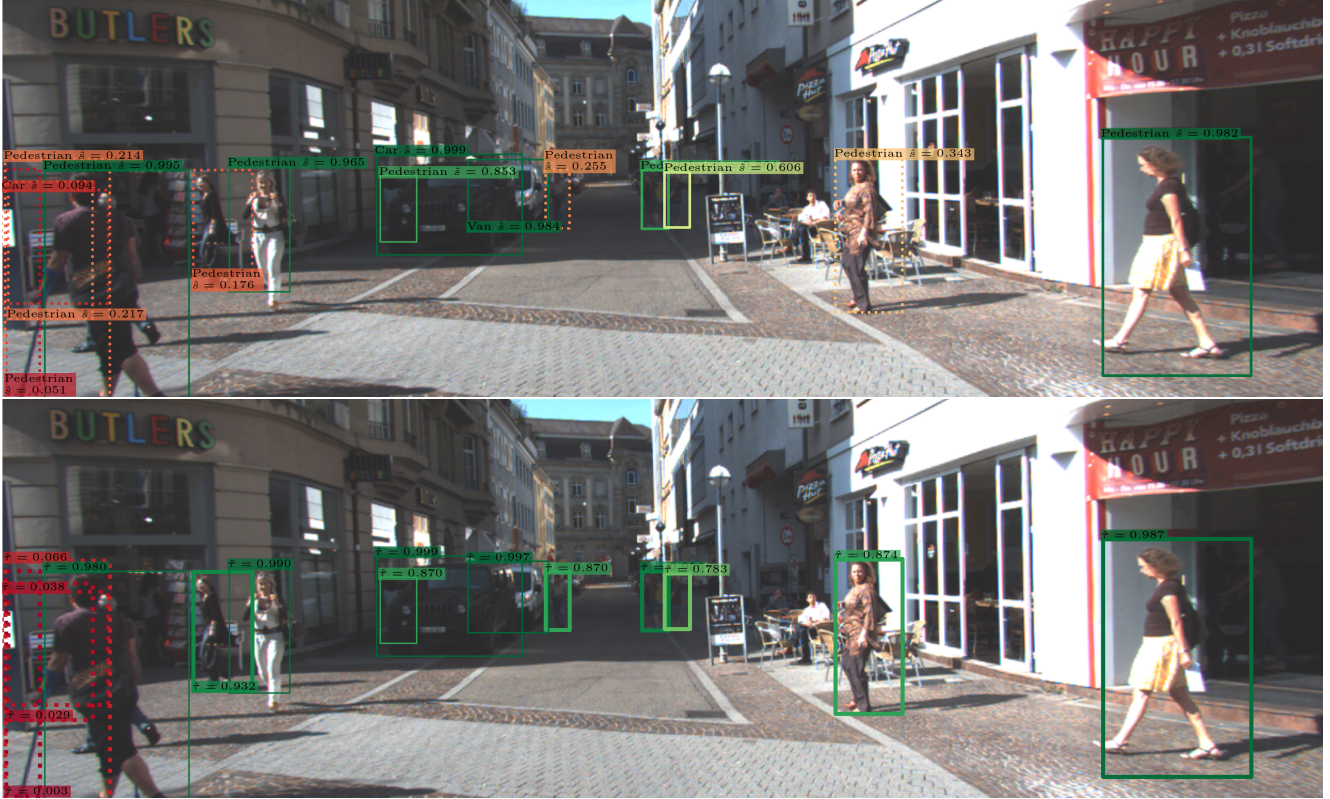


Figure 6. Full version of confidence estimation example in Fig. 1. Top: DNN Score \hat{s} ; bottom: meta classification confidence \hat{r} involving gradient metrics. True predictions with low confidence are assigned large meta classification confidences while false predictions are assigned low values. This allows for improved filtering based on confidence.

A.4. Calibration.

Generally, “calibration” methods (or re-calibration) aim at rectifying scores as confidences in the sense of Sec. 1 such that the calibrated scores reflect the conditional frequency of true predictions. For example, out of 100 predictions with a confidence of 0.3, around 30 should be correct.

Confidence calibration methods have been applied to object detection in [39] where temperature scaling was found to improve calibration. In addition to considering the expected calibration error (*ECE*) and the maximum calibration error (*MCE*) [38], the authors of [39] argue that in object detection, it is important that confidences are calibrated irrespective of how many examples fall into a bin. Therefore, they introduced the average calibration error (*ACE*) as a new calibration metric which is insensitive to the bin counts. The authors of [24] introduce natural extensions to localization-dependent calibration methods and a localization-dependent metric to measure calibration for different image regions.

In Sec. 5, we evaluated the calibration of meta classifiers in terms of the maximum (*MCE*, [38]) and average (*ACE*, [39]) calibration error which we define here. We sort the

examples into bins β_i , $i = 1, \dots, B$ of a fixed width (in our case 0.1, refer to Sec. 5) according to their confidence. For each bin β_i , we compute

$$\text{acc}_i = \frac{\text{TP}_i}{|\beta_i|}, \quad \text{conf}_i = \frac{1}{|\beta_i|} \sum_{j=1}^{|\beta_i|} \hat{c}_i \quad (12)$$

where $|\beta_i|$ denotes the number of examples in β_i and \hat{c}_i is the respective confidence, *i.e.*, the network’s score or a meta classification probability. TP_i denotes the number of correctly classified in β_i . In standard classification tasks, this boils down to the classification accuracy, whereas in the object detection setting, this is the detectors precision in the bin β_i . A meta classifier performs a binary classification on detector positives, so we keep with the notation used for classifiers. Calibration metrics are usually defined as functions of the bin-wise differences between acc_i and conf_i . In particular, we investigate the following calibration error metrics:

$$\text{MCE} = \max_{i=1, \dots, B} |\text{acc}_i - \text{conf}_i|, \quad (13)$$

$$ACE = \frac{1}{B} \sum_{i=1}^B |\text{acc}_i - \text{conf}_i|, \quad (14)$$

$$ECE = \frac{1}{B} \sum_{i=1}^B \frac{B}{|\beta_i|} |\text{acc}_i - \text{conf}_i|. \quad (15)$$

Table 13 also shows the expected (ECE , [38]) calibration error which was argued in [39] to be biased toward bins with large amounts of examples. ECE is, thus, less informative for safety-critical investigations.

B. Implemented Loss Functions

Here, we give a short account of the loss functions implemented in our experiments.

YOLOv3. The loss function we used to train YOLOv3 has the following terms:

$$\begin{aligned} \mathcal{L}_\xi^{\text{Yv3}}(\hat{y}, y) = & 2 \sum_{a=1}^{N_{\text{out}}} \sum_{t=1}^{N_{\text{a}}} \mathbb{I}_{at}^{\text{obj}} \cdot \left[\text{MSE} \left(\left(\begin{array}{c} \tilde{\tau}_w^a \\ \tilde{\tau}_h^a \end{array} \right), \left(\begin{array}{c} \tau_w^t \\ \tau_h^t \end{array} \right) \right) \right. \\ & \left. + \text{BCE} \left(\sigma \left(\begin{array}{c} \tilde{\tau}_x^a \\ \tilde{\tau}_y^a \end{array} \right), \sigma \left(\begin{array}{c} \tau_x^t \\ \tau_y^t \end{array} \right) \right) \right], \end{aligned} \quad (16)$$

$$\begin{aligned} \mathcal{L}_s^{\text{Yv3}}(\tilde{y}, y) = & \sum_{a=1}^{N_{\text{out}}} \sum_{t=1}^{N_{\text{a}}} \left[\mathbb{I}_{at}^{\text{obj}} \text{BCE}_a(\sigma(\tilde{\tau}_s), \mathbf{1}_{N_{\text{out}}}) \right. \\ & \left. + \mathbb{I}_{at}^{\text{noobj}}(y) \text{BCE}_a(\sigma(\tilde{\tau}_s), \mathbf{0}_{N_{\text{out}}}) \right], \end{aligned} \quad (17)$$

$$\mathcal{L}_p^{\text{Yv3}}(\tilde{y}, y) = \sum_{a=1}^{N_{\text{out}}} \sum_{t=1}^{N_{\text{a}}} \mathbb{I}_{at}^{\text{obj}} \text{BCE}(\sigma(\tilde{\tau}_p^a), \sigma(\tau_p^t)). \quad (18)$$

Here, the first sum ranges over all N_{out} anchors a and the second sum over the total number N_{gt} of ground truth instances in y . MSE is the usual mean squared error (Eq. (21)) for the regression of the bounding box size. As introduced in [43], the raw network outputs (in the notation of Theorem 1 this is one component $(\phi_T^c)_{ab}$ of the final feature map ϕ_T , see also Appendix D) for one anchor denoted by

$$\tilde{\tau} = (\tilde{\tau}_x, \tilde{\tau}_y, \tilde{\tau}_w, \tilde{\tau}_h, \tilde{\tau}_s, \tilde{\tau}_{p_1}, \dots, \tilde{\tau}_{p_C}) \quad (19)$$

are transformed to yield the components of \tilde{y} :

$$\begin{aligned} \tilde{x} &= \ell \cdot \sigma(\tilde{\tau}_x) + c_x, & \tilde{y} &= \ell \cdot \sigma(\tilde{\tau}_y) + c_y, & \tilde{w} &= \pi_w \cdot e^{\tilde{\tau}_w}, \\ \tilde{h} &= \pi_h \cdot e^{\tilde{\tau}_h}, & \tilde{s} &= \sigma(\tilde{\tau}_s), & \tilde{p}_j &= \sigma(\tilde{\tau}_{p_j}). \end{aligned} \quad (20)$$

Here, ℓ is the respective grid cell width/height, σ denotes the sigmoid function, c_x and c_y are the top left corner position of the respective cell and π_w and π_h denote the width and height of the bounding box prior (anchor). These relationships can be (at least numerically) inverted to transform ground truth boxes to the scale of $\tilde{\tau}$. We denote by

$\tau = (\tau_x, \tau_y, \tau_w, \tau_h, \tau_s, \tau_{p_1}, \dots, \tau_{p_C})$ that transformation of the (real) ground truth y which is collected in a feature map γ . Then, we have

$$\text{MSE}(\tilde{\tau}, \tau) = \sum_i (\tilde{\tau}_i - \tau_i)^2. \quad (21)$$

Whenever summation indices are not clearly specified, we assume from the context that they take on all possible values, *e.g.* in Eq. (16) w and h . Similarly, the binary cross entropy BCE is related to the usual cross entropy loss CE which is commonly used for learning probability distributions:

$$\begin{aligned} \text{BCE}(p, q) &= \sum_i \text{BCE}_i(p, q) \\ &= - \sum_i q_i \log(p_i) + (1 - q_i) \log(1 - p_i), \end{aligned} \quad (22)$$

$$\text{CE}(p, q) = - \sum_i q_i \log(p_i) \quad (23)$$

where $p, q \in (0, 1)^d$ for some fixed length $d \in \mathbb{N}$. Using binary cross entropy for classification amounts to learning C binary classifiers, in particular the ‘‘probabilities’’ \tilde{p}_j are in general not normalized. Note also, that each summand in Eq. (17) only has one contribution due to the binary ground truth $\mathbf{1}_{N_{\text{out}}}$, resp. $\mathbf{0}_{N_{\text{out}}}$. The binary cross entropy is also sometimes used for the center location of anchor boxes when the position within each cell is scaled to $(0, 1)$, see $\mathcal{L}_\xi^{\text{YOLOv3}}$.

The tensors \mathbb{I}^{obj} and $\mathbb{I}^{\text{noobj}}$ indicate whether anchor a can be associated to ground truth instance t (obj) or not (noobj) which is determined as in [44] from two thresholds $\varepsilon_+ \geq \varepsilon_- \geq 0$ which are set to 0.5 in our implementation.

Note, that both, \mathbb{I}^{obj} and $\mathbb{I}^{\text{noobj}}$ only depend on the ground truth y and the fixed anchors, but not on the output regression results \tilde{y} or the predictions \hat{y} .

We express a tensor with entries 1 with the size N as $\mathbf{1}_N$ and a tensor with entries 0 as $\mathbf{0}_N$. The ground truth t one-hot class vector is $\sigma(\tau_p^t) := p^t = (\delta_{i, \kappa_t})_{i=1}^C$.

Faster R-CNN and Cascade R-CNN. Since Faster R-CNN [44] and Cascade R-CNN [1] are two-stage architectures, there are separate loss contributions for the Region Proposal Network (RPN) and the Region of Interest (RoI) head, the latter of which produces the actual proposals. Formally, writing $\theta_\xi := (\theta_x, \theta_y, \theta_w, \theta_h)$ for the respectively transformed ground truth localization, similarly $\tilde{\theta}_\xi$ for the RPN outputs \tilde{y}^{RPN} and $\tilde{\theta}_s$ the proposal score output (where

$\tilde{s}^a = \sigma(\tilde{\theta}_s^a)$ is the proposal score):

$$\mathcal{L}_\xi^{\text{RPN}}(\tilde{y}^{\text{RPN}}, y) = \frac{1}{|I^+|} \sum_{a=1}^{N_{\text{out}}^{\text{RPN}}} \sum_{t=1}^{N_{\mathbf{x}}} I_a^+ \tilde{\mathbb{I}}_{at}^{\text{obj}} \text{sm}L_\beta^1(\tilde{\theta}_\xi^a, \theta_\xi^t), \quad (24)$$

$$\begin{aligned} \mathcal{L}_s^{\text{RPN}}(\tilde{y}^{\text{RPN}}, y) = & \sum_{a=1}^{N_{\text{out}}^{\text{RPN}}} \sum_{t=1}^{N_{\mathbf{x}}} \left[\mathbb{I}_{at}^{\text{obj}} \text{BCE}_a(\sigma(\tilde{\theta}_s), \mathbf{1}_{N_{\text{out}}^{\text{RPN}}}) \right. \\ & \left. + I_a^- \tilde{\mathbb{I}}_{at}^{\text{noobj}} \text{BCE}_a(\sigma(\tilde{\theta}_s), \mathbf{0}_{N_{\text{out}}^{\text{RPN}}}) \right]. \end{aligned} \quad (25)$$

The tensors $\tilde{\mathbb{I}}^{\text{obj}}$ and $\tilde{\mathbb{I}}^{\text{noobj}}$ are determined as for YOLOv3 with $\varepsilon_+ = 0.7$ and $\varepsilon_- = 0.3$) but we omit their dependence on y in our notation. Predictions are randomly sampled to contribute to the loss function by the tensors I^+ and I^- , which can be regarded as random variables. The constant batch size b of predictions to enter the RPN loss is a hyperparameter set to 256 in our implementation. We randomly sample $n_+ := \min\{|\tilde{\mathbb{I}}^{\text{obj}}|, b/2\}$ of the $|\tilde{\mathbb{I}}^{\text{obj}}|$ positive anchors (constituting the mask I^+) and $n_- := \min\{|\tilde{\mathbb{I}}^{\text{noobj}}|, b - n_+\}$ negative anchors (I^-). The summation of a ranges over the $N_{\text{out}}^{\text{RPN}}$ outputs of the RPN (in our case, 1000). Proposal regression is done based on the smooth L^1 loss

$$\text{sm}L_\beta^1(\tilde{\theta}, \theta) := \sum_i \left\{ \begin{array}{l} \frac{1}{2} |\tilde{\theta}_i - \theta_i|^2 \quad \left| \begin{array}{l} |\tilde{\theta}_i - \theta_i| < \beta \\ |\tilde{\theta}_i - \theta_i| - \frac{\beta}{2} \end{array} \right. \\ |\tilde{\theta}_i - \theta_i| - \frac{\beta}{2} \quad \left| \begin{array}{l} |\tilde{\theta}_i - \theta_i| \geq \beta \end{array} \right. \end{array} \right. , \quad (26)$$

where we use the default parameter choice $\beta = \frac{1}{9}$. The final prediction \hat{y} of Faster R-CNN is computed from the proposals and RoI results¹ $\tilde{\tau}$ in the RoI head:

$$\begin{aligned} \tilde{x} &= \pi_w \cdot \tilde{\tau}_x + \pi_x, & \tilde{y} &= \pi_y \cdot \tilde{\tau}_y + \pi_y, \\ \tilde{w} &= \pi_w \cdot e^{\tilde{\tau}_w}, & \tilde{h} &= \pi_h \cdot e^{\tilde{\tau}_h}, & \tilde{p} &= \Sigma(\tilde{\tau}_p), \end{aligned} \quad (27)$$

where $\Sigma^i(x) := e^{x_i} / \sum_j e^{x_j}$ is the usual softmax function and $\pi := (\pi_x, \pi_y, \pi_w, \pi_h)$ is the respective proposal localization. Denoting with $\tau_\xi := (\tau_x, \tau_y, \tau_w, \tau_h)$ ground truth localization transformed relatively to the respective proposal:

$$\mathcal{L}_\xi^{\text{RoI}}(\tilde{y}, y) = \frac{1}{|\mathbb{I}^{\text{obj}}|} \sum_{a=1}^{N_{\text{out}}} \sum_{t=1}^{N_{\mathbf{x}}} \mathbb{I}_{at}^{\text{obj}} \text{sm}L_\beta^1(\tilde{\tau}_\xi^a, \tau_\xi^t), \quad (28)$$

$$\begin{aligned} \mathcal{L}_p^{\text{RoI}}(\tilde{y}, y) = & \sum_{a=1}^{N_{\text{out}}} \sum_{t=1}^{N_{\mathbf{x}}} \left[\mathbb{I}_{at}^{\text{obj}} \text{CE}(\Sigma(\tilde{\tau}_p^a), p^t) \right. \\ & \left. + \mathbb{I}_{at}^{\text{noobj}} \text{CE}(\Sigma(\tilde{\tau}_{p_0}^a), 1) \right]. \end{aligned} \quad (29)$$

¹The result $\tilde{\tau}$ is similar to Eq. (19), but without $\tilde{\tau}_s$ where we have instead $C+1$ classes, with one ‘‘background’’ class. We denote the respective probability by \tilde{p}_0 .

Here, \mathbb{I}^{obj} and $\mathbb{I}^{\text{noobj}}$ are computed with $\varepsilon_+ = \varepsilon_- = 0.5$. The cascaded bounding box regression of Cascade R-CNN implements the smooth L^1 loss at each of three cascade stages, where bounding box offsets and scaling are computed from the previous bounding box regression results as proposals.

RetinaNet. In the RetinaNet [26] architecture, score assignment is part of the classification.

$$\mathcal{L}_\xi^{\text{Ret}}(\tilde{y}, y) = \frac{1}{|\mathbb{I}^{\text{obj}}|} \sum_{a=1}^{N_{\text{out}}} \sum_{t=1}^{N_{\mathbf{x}}} \mathbb{I}_{at}^{\text{obj}} L^1(\tilde{\tau}_\xi^a, \tau_\xi^t), \quad (30)$$

$$\begin{aligned} \mathcal{L}_p^{\text{Ret}}(\tilde{y}, y) = & \frac{1}{|\mathbb{I}^{\text{obj}}|} \sum_{a=1}^{N_{\text{out}}} \sum_{t=1}^{N_{\mathbf{x}}} \left[\mathbb{I}_{at}^{\text{obj}} \sum_{j=1}^C \alpha (1 - \sigma(\tilde{\tau}_{p_j}^a))^{\gamma_F} \right. \\ & \cdot \text{BCE}_j(\sigma(\tilde{\tau}_p^a), p^t) \\ & \left. + \mathbb{I}_{at}^{\text{noobj}} (1 - \alpha) \sigma(\tilde{\tau}_{p_0}^a)^{\gamma_F} \cdot \text{BCE}(\sigma(\tilde{\tau}_{p_0}^a), 0) \right]. \end{aligned} \quad (31)$$

For \mathbb{I}^{obj} and $\mathbb{I}^{\text{noobj}}$, we use $\varepsilon_+ = 0.5$ and $\varepsilon_- = 0.4$. Regression is based on the absolute loss $L^1(\tilde{\tau}, \tau) = \sum_i |\tilde{\tau}_i - \tau_i|$ and the classification loss is a formulation of the well-known focal loss with $\alpha = 0.25$ and $\gamma_F = 2$. Bounding box transformation follows the maps in Eq. (27), where π are the respective RetinaNet anchor localizations instead of region proposals. The class-wise scores of the prediction are obtained by $\tilde{p}_j = \sigma(\tilde{\tau}_{p_j})$, $j = 1, \dots, C$ as for YOLOv3.

Theoretical loss derivatives. Here, we symbolically compute the loss gradients w.r.t. the network outputs as obtained from our accounts of the loss functions in the previous paragraphs. We do so in order to determine the computational complexity for $D_1 \mathcal{L}|_{\phi_T}$ in Appendix D. Note, that for all derivatives of the cross entropy, we can use

$$\frac{d}{d\tau} [-y \log(\sigma(\tau)) - (1 - y) \log(1 - \sigma(\tau))] = \sigma(\tau) - y. \quad (32)$$

We then find for $b = 1, \dots, N_{\text{out}}$ and features $r \in \{x, y, w, h, s, p_1, \dots, p_C\}$

$$\frac{\partial}{\partial \tilde{\tau}_r^b} \mathcal{L}_\xi^{\text{Yv3}} = 2 \sum_{t=1}^{N_{\mathbf{x}}} \mathbb{I}_{bt}^{\text{obj}} \left\{ \begin{array}{l} \tilde{\tau}_r^b - \tau_r^t \\ \sigma(\tilde{\tau}_r^b) - \sigma(\tau_r^t) \\ 0 \end{array} \right| \begin{array}{l} r \in \{w, h\} \\ r \in \{x, y\} \\ \text{otherwise.} \end{array}, \quad (33)$$

$$\frac{\partial}{\partial \tilde{\tau}_r^b} \mathcal{L}_s^{\text{Yv3}} = \delta_{rs} \sum_{t=1}^{N_{\mathbf{x}}} \left[\mathbb{I}_{bt}^{\text{obj}} (\tilde{s}^b - 1) + \mathbb{I}_{bt}^{\text{noobj}} \tilde{s}^b \right], \quad (34)$$

$$\frac{\partial}{\partial \tilde{\tau}_r^b} \mathcal{L}_p^{\text{Yv3}} = \sum_{t=1}^{N_{\mathbf{x}}} \mathbb{I}_{bt}^{\text{obj}} \sum_{i=1}^C \delta_{r p_i} (\tilde{p}_i^b - p_i^t), \quad (35)$$

where δ_{ij} is the Kronecker symbol, i.e., $\delta_{ij} = 1$ if $i = j$ and 0 otherwise. Further, with analogous notation for the output variables of RPN and RoI

$$\frac{\partial}{\partial \hat{\theta}_r^b} \mathcal{L}_\xi^{\text{RPN}} = \frac{1}{|I^+|} \sum_{t=1}^{N_{\mathbf{x}}} I_b^+ \tilde{\mathbb{I}}_{bt}^{\text{obj}} \cdot \begin{cases} \hat{\theta}_r^b - \theta_r^t & \left| \begin{array}{l} |\hat{\theta}_r^b - \theta_r^t| < \beta \text{ and} \\ r \in \{x, y, w, h\} \end{array} \right. \\ \text{sgn}(\hat{\theta}_r^b - \theta_r^t) & \left| \begin{array}{l} |\hat{\theta}_r^b - \theta_r^t| \geq \beta \text{ and} \\ r \in \{x, y, w, h\} \end{array} \right. \\ 0 & \text{otherwise} \end{cases}, \quad (36)$$

$$\frac{\partial}{\partial \hat{\theta}_r^b} \mathcal{L}_s^{\text{RPN}} = \delta_{rs} \left[I_b^+ \tilde{\mathbb{I}}_{bt}^{\text{obj}} (\hat{s}^b - 1) + I_b^- \tilde{\mathbb{I}}_{bt}^{\text{noobj}} \hat{s}^b \right]. \quad (37)$$

Here, sgn denotes the sign function, which is the derivative of $|\cdot|$ except for the origin. Similarly,

$$\frac{\partial}{\partial \hat{\tau}_r^b} \mathcal{L}_\xi^{\text{RoI}} = \frac{1}{|\mathbb{I}^{\text{obj}}|} \sum_{t=1}^{N_{\mathbf{x}}} \mathbb{I}_{bt}^{\text{obj}} \cdot \begin{cases} \hat{\tau}_r^b - \tau_r^t & \left| \begin{array}{l} |\hat{\tau}_r^b - \tau_r^t| < \beta \text{ and} \\ r \in \{x, y, w, h\} \end{array} \right. \\ \text{sgn}(\hat{\tau}_r^b - \tau_r^t) & \left| \begin{array}{l} |\hat{\tau}_r^b - \tau_r^t| \geq \beta \text{ and} \\ r \in \{x, y, w, h\} \end{array} \right. \\ 0 & \text{otherwise} \end{cases}, \quad (38)$$

$$\frac{\partial}{\partial \hat{\tau}_r^b} \mathcal{L}_p^{\text{RoI}} = - \sum_{t=1}^{N_{\mathbf{x}}} \left[\mathbb{I}_{bt}^{\text{obj}} \sum_{j=1}^C p_j^t \left(\delta_{p_j r} - \sum_{k=0}^C \delta_{p_k r} \Sigma^k(\hat{\tau}_p^b) \right) + \mathbb{I}_{bt}^{\text{noobj}} \left(\delta_{p_0 r} - \sum_{k=0}^C \delta_{p_k r} \Sigma^k(\hat{\tau}_p^b) \right) \right]. \quad (39)$$

Note that the inner sum over j only has at most one term due to $\delta_{p_j r}$. With $\sigma'(\tau) = \sigma(\tau)(1 - \sigma(\tau))$, we finally find for RetinaNet

$$\frac{\partial}{\partial \hat{\tau}_r^b} \mathcal{L}_\xi^{\text{Ret}} = \frac{1}{|\mathbb{I}^{\text{obj}}|} \sum_{t=1}^{N_{\mathbf{x}}} \mathbb{I}_{bt}^{\text{obj}} \cdot \begin{cases} \text{sgn}(\hat{\tau}_r^b - \tau_r^t) & r \in \{x, y, w, h\} \\ 0 & \text{otherwise} \end{cases}, \quad (40)$$

$$\frac{\partial}{\partial \hat{\tau}_r^b} \mathcal{L}_p^{\text{Ret}} = \frac{1}{|\mathbb{I}^{\text{obj}}|} \sum_{t=1}^{N_{\mathbf{x}}} \left[\mathbb{I}_{bt}^{\text{obj}} \sum_{j=1}^C \delta_{p_j r} \alpha (1 - \sigma(\hat{\tau}_{p_j}^b))^{\gamma_F} \cdot [-\gamma_F \sigma(\hat{\tau}_{p_j}^b) \text{BCE}_j(\sigma(\hat{\tau}_{p_j}^b), p^t) + \sigma(\hat{\tau}_{p_j}^b) - 1] + \mathbb{I}_{bt}^{\text{noobj}} \delta_{p_0 r} (1 - \alpha) \sigma(\hat{\tau}_{p_0}^b)^{\gamma_F} \cdot [-\gamma_F (1 - \sigma(\hat{\tau}_{p_0}^b)) \log(1 - \sigma(\hat{\tau}_{p_0}^b)) + \sigma(\hat{\tau}_{p_0}^b)] \right]. \quad (41)$$

Table 5. Dataset splits used for training and evaluation.

Dataset	training	evaluation	# eval images
VOC	2007+2012 trainval	2007 test	4952
COCO	train2017	val2017	5000
KITTI	random part of training	complement part of training	2000

C. Implementation details

Here, we state details of the implementations of our framework to different architectures, and on different datasets.

C.1. Datasets

In order to show a wide range of applications, we investigate our method on the following object detection datasets (see Tab. 5 for the splits used).

Pascal VOC 2007+2012 [8]. The Pascal VOC dataset is an object detection benchmark of everyday images involving 20 different object categories. We train on the 2007 and 2012 trainval splits, accumulating to 16550 train images and we evaluate on the 2007 test split of 4952 images. For training, we include labels marked as “difficult” in the original annotations.

MS COCO 2017 [27]. The MS COCO dataset constitutes a second vision benchmark involving 2D bounding box detection annotations for everyday images with 80 object categories. We train on the train2017 split of 118287 images and evaluate on the 5000 images of the val2017 split.

KITTI [11]. The KITTI vision benchmark contains 21 real world street scenes annotated with 2D bounding boxes. We randomly divide the 7481 labeled images into a training split of 5481 images and use the complement of 2000 images for evaluation.

C.2. Detectors

For our experiments, we employ three common object detection architectures, namely YOLOv3 with Darknet53 backbone [43], Faster R-CNN [44] and RetinaNet [26], each with a ResNet50FPN [15] backbone. Moreover, we investigate a state-of-the-art detector in Cascade R-CNN [1] with a large ResNeSt200FPN [56] backbone. We started from PyTorch [41] reimplementations, added dropout layers and trained from scratch on the datasets in Tab. 5. We list some of the detector-specific details.

YOLOv3. The basis of our implementation is a publicly available GitHub repository [54]. We position dropout lay-

ers with $p = 0.5$ before the last convolutional layers of each detection head. Gradient metrics are computed over the last two layers in each of the three detection heads as the final network layers have been found to be most informative in the classification setting [40]. Since each output box is the result of exactly one of the three heads, we only have two layers for gradients per box resulting in 2×3 gradients per box (2 layers per 3 losses) as indicated in Tab. 1. We train an ensemble of 5 detectors for each dataset from scratch.

Faster R-CNN. Based on the official Torchvision implementation, our model uses dropout ($p = 0.5$) before the last fully connected layer of the architecture (classification and bounding box prediction in the Fast R-CNN head). We compute gradient metrics for the last two fully connected layers of the Fast R-CNN head as well as for the last two convolutional layers of the RPN per box (objectness and localization), leading to 4×2 gradients per box (2 + 2 for localization, 2 for classification and 2 for proposal objectness).

RetinaNet. We also employ RetinaNet as implemented in Torchvision with ($p = 0.5$)-dropout before the last convolutional layers for bounding box regression and classification. Gradients are computed for the last two convolutional layers for bounding box regression and classification resulting in 2×2 gradients per prediction.

Cascade R-CNN. We use the Detectron2 [55]-supported implementation of ResNeSt provided by the ResNeSt authors Zhang *et al.* [56] and the pre-trained weights on the MS COCO dataset. We train from scratch on Pascal VOC and KITTI. Since this model is primarily interesting for investigation due to its naturally strong score baseline based on cascaded regression, we do not report MC dropout results for it. Gradient uncertainty metrics are computed for the last two fully connected layers (bounding box regression and classification) of each of the three cascades. The loss of later cascade stages depends in principle on the weights of previous cascade stages. However, we only compute the gradients with respect to the weights in the current stage resulting in 2×6 (3 stages for bounding box regression and classification) gradients for the Cascade R-CNN head. Furthermore, we have the 2×2 RPN gradients as in Faster R-CNN.

C.3. Uncertainty baselines

We give a short account of the baselines implemented and investigated in our experiments.

Score. By the score, we mean the box-wise objectness score for YOLOv3 and the maximum softmax probability for Faster R-CNN, RetinaNet and Cascade R-CNN. As

Table 6. Ablation on the temperature parameter T for the energy score in terms of meta classification ($AuROC$ and AP) and meta regression (R^2).

	$AuROC$	AP	R^2
$T = 1$	92.52 ± 0.03	91.86 ± 0.04	62.12 ± 0.09
$T = 10$	78.42 ± 0.13	81.75 ± 0.08	32.92 ± 0.20
$T = 100$	95.66 ± 0.02	95.33 ± 0.03	71.79 ± 0.06
$T = 1000$	95.62 ± 0.03	95.33 ± 0.04	71.78 ± 0.05
Score	96.53 ± 0.05	96.87 ± 0.03	78.86 ± 0.05
MD	98.23 ± 0.02	98.06 ± 0.02	85.88 ± 0.10
GS _{full}	<u>98.04 ± 0.03</u>	<u>97.81 ± 0.06</u>	<u>85.40 ± 0.11</u>

standard object detection pipelines discard output bounding boxes based on a score threshold, this quantity is the baseline for discriminating true against false outputs.

Entropy. The entropy is a common “hand-crafted” uncertainty measure based on the classification output $\tilde{p} \in [0, 1]^C$ (softmax or category-wise sigmoid) and given by

$$H(\tilde{p}) = - \sum_{c=1}^C \tilde{p}_c \log(\tilde{p}_c). \quad (42)$$

Energy. As an alternative to the maximum softmax probability and the entropy, Liu *et al.* proposed an energy score depending on a temperature parameter T given by

$$E(\tilde{\tau}) = -T \log \sum_{c=1}^C e^{\tilde{\tau}_{p_c}/T} \quad (43)$$

based on the probability logits $(\tilde{\tau}_{p_1}, \dots, \tilde{\tau}_{p_C})$. We found that $T = 100$ delivers the strongest results, see Tab. 6 where we compared different values of T (like in [29]) for YOLOv3 on the KITTI dataset in terms of meta classification and meta regression performance.

Full softmax. We investigate an enveloping model of all classification-based uncertainty metrics by involving all probabilities $(\tilde{p}_1, \dots, \tilde{p}_C)$ directly as co-variables in the meta classifier or meta regression model. We find that it outperforms all purely classification-based models, which is expected.

MC dropout (MC). As a common baseline, we investigate Monte-Carlo dropout uncertainty. Since we are explicitly interested in the uncertainty content of MC dropout, we only include anchor-wise standard deviations of the entire network output \tilde{y} obtained from 30 dropout samples. We found that computing more samples does not significantly improve predictive uncertainty content as seen in the ablation study on the MC sample count N_{MC} in Tab. 7 for

Table 7. Ablation on the sample count size N_{MC} for MC dropout in terms of meta classification ($AuROC$ and AP) and meta regression (R^2). Results obtained from the sample standard deviation.

	$AuROC$	AP	R^2
$N_{MC} = 10$	97.40 ± 0.04	96.91 ± 0.06	80.85 ± 0.10
$N_{MC} = 15$	97.50 ± 0.03	97.08 ± 0.07	81.28 ± 0.09
$N_{MC} = 20$	97.69 ± 0.03	97.28 ± 0.05	82.11 ± 0.09
$N_{MC} = 25$	97.64 ± 0.03	97.20 ± 0.04	81.94 ± 0.12
$N_{MC} = 30$	97.60 ± 0.07	97.17 ± 0.10	82.10 ± 0.11
$N_{MC} = 35$	97.71 ± 0.03	97.29 ± 0.05	82.17 ± 0.13
$N_{MC} = 40$	97.69 ± 0.04	97.29 ± 0.06	82.12 ± 0.13
Score	96.53 ± 0.05	96.87 ± 0.03	78.86 ± 0.05
MD	98.23 ± 0.02	98.06 ± 0.02	85.88 ± 0.10
GS _{full}	98.04 ± 0.03	97.81 ± 0.06	85.40 ± 0.11

Table 8. Ablation on the ensemble size N_{ens} for deep ensembles in terms of meta classification ($AuROC$ and AP) and meta regression (R^2). Results obtained from the sample standard deviation.

	$AuROC$	AP	R^2
$N_{ens} = 3$	97.53 ± 0.03	97.17 ± 0.05	82.63 ± 0.13
$N_{ens} = 4$	97.79 ± 0.04	97.48 ± 0.06	83.62 ± 0.12
$N_{ens} = 5$	97.92 ± 0.04	97.63 ± 0.05	84.18 ± 0.12
$N_{ens} = 6$	98.04 ± 0.03	97.75 ± 0.04	84.64 ± 0.16
$N_{ens} = 7$	98.06 ± 0.03	97.80 ± 0.05	84.78 ± 0.11
$N_{ens} = 8$	<u>98.08 ± 0.02</u>	97.80 ± 0.03	84.91 ± 0.10
Score	96.53 ± 0.05	96.87 ± 0.03	78.86 ± 0.05
MD	98.23 ± 0.02	98.06 ± 0.02	85.88 ± 0.10
GS _{full}	98.04 ± 0.03	<u>97.81 ± 0.06</u>	85.40 ± 0.11

YOLOv3 on the KITTI dataset. Meta classification performance can be further improved by involving dropout means of \tilde{y} . However, MC dropout means do not carry an intrinsic meaning of uncertainty as opposed to standard deviations, so we do not include them in our main experiments.

Deep ensembles (E). As another common, sampling-based baseline, we investigate deep ensemble uncertainty obtained from ensembles of size 5. We find that larger ensembles do not significantly improve meta classification performance. For reference, we show an ablation on the ensemble size N_{ens} for YOLOv3 on the KITTI dataset in Tab. 8 in terms of meta classification and meta regression. By the same motivation like for MC dropout, we only include anchor-wise standard deviations over forward passes from the ensemble.

MetaDetect (MD). The output-based MetaDetect framework computes uncertainty metrics for use in meta classification and meta regression from pre-NMS variance in anchor-based object detection. In our implementation, we

compute the $46 + C$ (where C is the number of categories) MetaDetect metrics [48] which include the entire network output \tilde{y} . The MetaDetect framework is, therefore, an enveloping model to any uncertainty metrics based on the object detection output (in particular to any classification-based uncertainty) which we also find in our experiments. We include it in order to cover all such baselines.

Details of gradient-based uncertainty (GS). In our experiments, we investigate two gradient-based uncertainty models. While $GS_{\|\cdot\|_2}$ is based on the two-norms of box-wise gradients, GS_{full} utilizes all the six maps in Eq. (3). While the two norms $\|\cdot\|_1$ and $\|\cdot\|_2$ directly compute the magnitude of a vector, the maps $mean(\cdot)$ and $std(\cdot)$ do not immediately capture a concept of length. However, they have been found in [40] to yield decent separation capabilities. Similarly, the component-wise $min(\cdot)$ and $max(\cdot)$ contain relevant predictive information. Note, that the latter two are related to the sup-norm $\|\cdot\|_\infty$ but together contain more information. While the last layer gradients themselves are highly informative, we allow for gradients of the last two layers in our main experiments. In Tab. 9 we show meta classification and meta regression performance of gradient-based models with metrics obtained from different numbers of network layers of the YOLOv3 model on the KITTI dataset. Starting with the last layer gradient only (# layers is 1), the gradient metrics from the two last layers and so on. We see that meta classification performance quickly saturates and no significant benefit can be seen from using more than 3 layers. However, meta regression can still be improved slightly by using up to 5 network layers.

Throughout our experiments, we compute gradients via the PyTorch autograd framework, iteratively for each bounding box. This procedure is computationally far less efficient than directly computing the gradients from the formulas in Appendix B. We show in Appendix D, that the latter is, in fact, at worst similar in FLOP count to MC dropout or deep sub-ensembles (an efficient implementation of deep ensembles).

In order to save computational effort, we compute gradient metrics not for all predicted bounding boxes. We use a small score threshold of 10^{-4} (KITTI, Pascal VOC), respectively 10^{-2} (COCO) as a pre-filter. On average, this produces ~ 150 predictions per image. These settings lead to a highly disbalanced TP/FP ratio post NMS on which meta classification and meta regression models are fitted. On YOLOv3, for example, these ratios are for Pascal VOC: 0.099, MS COCO: 0.158 and for KITTI: 0.464, so our models fit on significantly more FPs than TPs. However, our meta classification and meta regression models (see Sec. 4) are gradient boosting models which tend to reflect well-calibrated confidences / regressions on the domain of training data. Our results (e.g. Tab. 2) obtained from cross-

Table 9. Ablation on the number of network layers used in terms of meta classification ($AuROC$ and AP) and meta regression (R^2). Gradient metrics per layer are accumulated to those of later layers starting from the last layer of the DNN.

Metric	Score	# layers				
		1	2	3	4	5
$AuROC$	96.53 ± 0.05	98.04 ± 0.03	98.06 ± 0.02	98.18 ± 0.03	98.18 ± 0.03	98.19 ± 0.02
AP	96.87 ± 0.03	97.81 ± 0.06	97.83 ± 0.04	97.98 ± 0.05	98.00 ± 0.04	98.04 ± 0.04
R^2	78.89 ± 0.05	84.35 ± 0.05	85.40 ± 0.11	86.04 ± 0.11	86.18 ± 0.07	86.24 ± 0.09

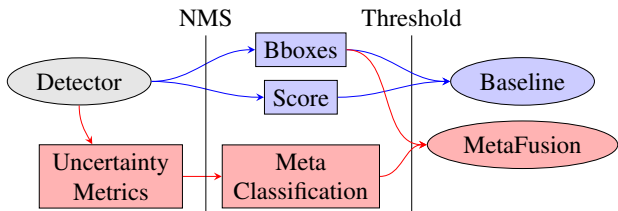


Figure 7. Schematic sketch of the baseline detection pipeline and the alternative MetaFusion pipeline for an object detector.

validation confirm that this ratio does not constitute an obstacle for obtaining well-performing models on data not used to fit the model. For gradient boosting models, we employ the XGBoost library [3] with 30 estimators (otherwise standard settings).

C.4. MetaFusion framework

In Sec. 5, we showed a way of trading uncertainty information for detection performance. Figure 7 shows a sketch of the resulting pipeline, where the usual object detection pipeline is shown in blue. The standard object detection pipeline relies on filtering out false positive output boxes on the basis of their score (see also Fig. 6). An altered confidence estimation like meta classification can improve the threshold-dependent detection quality of the object detection pipeline. This way, boxes which are falsely assigned a low score can survive the thresholding step. Similarly, FPs with a high score may be suppressed by proper predictive confidence estimation methods. This approach is not limited to meta classification, however, our experiments show that meta classification constitutes such a method.

D. Computational complexity

In this section, we discuss the details of the setting in which Theorem 1 was formulated and give a proof for the statements made there. The gradients for our uncertainty metrics are usually computed via backpropagation only for a few network layers. Therefore, we restrict ourselves to the setting of fully convolutional neural networks.

Setting. As in [49, Chapter 20.6], we regard a (convolutional) neural network as a graph of feature maps with vertices $V = \bigsqcup_{t=0}^T V_t$ arranged in layers V_t . For our consideration it will suffice to regard them as sequentially ordered. We denote $[n] := \{1, \dots, n\}$ for $n \in \mathbb{N}$. Each layer V_t contains a set number $k_t := |V_t|$ of feature map activations (channels) $\phi_t^c \in \mathbb{R}^{h_t \times w_t}$, $c \in [k_t]$. We denote the activation of V_t by $\phi_t = (\phi_t^1, \dots, \phi_t^{k_t})$. The activation $\phi_{t+1} \in (\mathbb{R}^{h_{t+1} \times w_{t+1}})^{k_{t+1}}$ is obtained from ϕ_t by convolutions. We have $k_t \times k_{t+1}$ quadratic filter matrices

$$(K_{t+1})_c^d \in \mathbb{R}^{(2s_t+1) \times (2s_t+1)}, \quad c \in [k_t]; \quad d \in [k_{t+1}], \quad (44)$$

where s_t is a (usually small) natural number, the spatial extent of the filter. Also, we have respectively k_{t+1} biases $b_{t+1}^d \in \mathbb{R}$, $d \in [k_{t+1}]$. The convolution (actually in most implementations, the cross correlation) of $K \in \mathbb{R}^{(2s+1) \times (2s+1)}$ and $\phi \in \mathbb{R}^{h \times w}$ is defined as

$$(K * \phi)_{ab} := \sum_{m,n=-s}^s K_{s+1+p,s+1+q} \phi_{a+p,b+q}, \quad (45)$$

where $a = 1, \dots, h$ and $b = 1, \dots, w$. This is, strictly speaking, only correct for convolutions with stride 1, although a closed form can be given for the more general case. For our goals, we will use stride 1 to upper bound the FLOPs which comes with the simplification that the feature maps' sizes are conserved. We then define

$$\psi_{t+1}^d = \sum_{c=1}^{k_t} (K_{t+1})_c^d * \phi_t^c + b_{t+1}^d \mathbf{1}_{h_t \times w_t}, \quad d \in [k_{t+1}]. \quad (46)$$

Finally, we apply activation functions $\alpha_t : \mathbb{R} \rightarrow \mathbb{R}$ to each entry to obtain $\phi_{t+1} = \alpha_{t+1}(\psi_{t+1})$. In practice, α_t is usually a ReLU activation, i.e., $\alpha_t(x) = \max\{x, 0\}$ or a slight modification (e.g. leaky ReLU) of it and we will treat the computational complexity of this operation later. We can then determine the computational expense of computing ψ_{t+1} from ϕ_t . In the following, we will be interested in the linear convolution action

$$C^{K_t} : \mathbb{R}^{k_{t-1} \times h_{t-1} \times w_{t-1}} \rightarrow \mathbb{R}^{k_t \times h_t \times w_t}, \quad (47)$$

$$(C^{K_t} \phi_{t-1})_{ab}^d := \left(\sum_{c=1}^{k_{t-1}} (K_t)_c^d * \phi_{t-1}^c \right)_{ab},$$

where $d \in [k_t]$, $a \in [h_t]$ and $b \in [w_t]$. Note that C^K is also linear in K_t . On the last layer feature map ϕ_T we define the loss function $\mathcal{L} : (\phi_T, \gamma) \mapsto \mathcal{L}(\phi_T, \gamma) \in \mathbb{R}$. Here, γ stands for the ground truth² transformed to feature map size $\mathbb{R}^{h_T \times w_T \times k_T}$. In order to make dependencies explicit, define the loss of the sub-net starting at layer t by ℓ_t , i.e.,

$$\ell_T(\phi_T) := \mathcal{L}(\phi_T, \gamma), \quad \ell_{t-1}(\phi_{t-1}) := \ell_t(\alpha_t(\psi_t)). \quad (48)$$

Straight-forward calculations yield

$$\begin{aligned} \nabla_{K_T} \mathcal{L} &= \nabla_{K_T} (\ell_T \circ \alpha_T \circ \psi_T(K_T)) \\ &= D_1 \mathcal{L}|_{\phi_T} \cdot D\alpha_T|_{\psi_T} \cdot \nabla_{K_T} \psi_T \\ \nabla_{K_{T-1}} \mathcal{L} &= \nabla_{K_{T-1}} (\ell_T \circ \alpha_T \circ \psi_T \circ \alpha_{T-1} \circ \psi_{T-1}(K_{T-1})) \\ &= D_1 \mathcal{L}|_{\phi_T} \cdot D\alpha_T|_{\psi_T} \cdot C^{K_T} \cdot \\ &\quad \cdot D\alpha_{T-1}|_{\psi_{T-1}} \cdot \nabla_{K_{T-1}} \psi_{T-1}. \end{aligned} \quad (50)$$

Here, D denotes the total derivative (D_1 for the first variable, resp.) and we have used the linearity of C^{K_T} . Note, that in Sec. 4, we omitted the terms $D\alpha_T|_{\psi_T}$ and $D\alpha_{T-1}|_{\psi_{T-1}}$. We will come back to them later in the discussion. For the gradient metrics we present in this paper, each \tilde{y}^j for which we compute gradients receives a binary mask μ^j such that $\mu^j \cdot \phi_T$ are the feature map representations of candidate boxes for \tilde{y}^j (see Appendix A). The scalar loss function then becomes $\mathcal{L}(\mu^j \phi_T, \gamma^j)$ for the purposes of computing gradient uncertainty, where γ^j is \bar{y}^j in feature map representation. We address next, how this masking influences Eq. (49), Eq. (50) and the FLOP count of our method.

Computing the mask. The complexity of determining μ^j (i.e., finding $\text{cand}[\tilde{y}^j]$) is the complexity of computing all mutual *IoU* values between \tilde{y}^j and the $n_T := h_T \cdot w_T \cdot k_T$ other predicted boxes. Computing the *IoU* of a box $b_1 = (x_1^{\min}, y_1^{\min}, x_1^{\max}, y_1^{\max})$ and $b_2 = (x_2^{\min}, y_2^{\min}, x_2^{\max}, y_2^{\max})$ can be done in a few steps with an efficient method exploiting the fact that:

$$U = A_1 + A_2 - I, \quad \text{IoU} = I/U, \quad (51)$$

where the computation of the intersection area I and the individual areas A_1 and A_2 can each be done in 3 FLOP, resulting in 12 FLOP per pair of boxes. Note that different localization constellations of b_1 and b_2 may result in slightly varying formulas for the computation of I but the constellation can be easily determined by binary checks which we ignore computationally. Also, the additional check for the class and sufficient score will be ignored, so we have $12n_T$ FLOP per mask μ^j . Inserting the binary mask³ μ^j in

²The transformations are listed in Appendix B for the entries τ of ϕ_T .

³See Sec. 4. The mask μ^j selects the feature map representation of $\text{cand}[\tilde{y}^j]$ out of ϕ_T .

Eq. (49) and Eq. (50) leads to the replacement of $D_1 \mathcal{L}|_{\phi_T} \cdot D\alpha_T|_{\psi_T}$ by $D\mathcal{L}^j := D_1 \mathcal{L}(\cdot, \gamma^j)|_{\mu^j \phi_T} \cdot \mu^j \cdot D\alpha_T|_{\psi_T}$ for each relevant box \tilde{y}^j .

In Tab. 10 we have listed upper bounds on the number of FLOP and elementary function evaluations performed for the computation of $D\mathcal{L}^j$ for the investigated loss functions. The numbers were obtained from the explicit partial derivatives computed in Appendix B. In principle, those formulas allow for every possible choice of $b \in [N_{\text{out}}]$ which is why all counts are proportional to it. Practically, however, at most the $|\mu^j|$ candidate boxes are relevant which need to be identified additionally as foreground or background for \tilde{y}^j in a separate step involving an *IoU* computation between \tilde{y}^j and the respective anchor. The total count of candidate boxes in practice is on average not larger than ~ 30 . When evaluating the formulas from Appendix B note, that there is only one ground truth box per gradient and we assume here, that one full forward pass has already been performed such that the majority of the appearing evaluations of elementary functions (sigmoids, exponentials, etc.) have been computed beforehand. This is not the case for the RetinaNet classification loss (41). In Tab. 10 we also list the additional post-processing cost for the output transformations (see Appendix B, Eqs. (20) and (27)) required for sampling-based uncertainty quantification like MC dropout or deep ensemble samples (“sampling pp”). The latter are also proportional to N_{out} , but also to the number N_{samp} of samples.

Proof of Theorem 1. Before we begin the proof, we first re-state the claims of Theorem 1.

Theorem 1. *The number of FLOP required to compute the last layer ($t = T$) gradient $\nabla_{K_T} \mathcal{L}(\mu^j \phi_T(K_T), \gamma^j)$ is $\mathcal{O}(k_T h w + k_T k_{T-1} (2s_T + 1)^4)$. Similarly, for earlier layers t , i.e., $\nabla_{K_t} \mathcal{L}(\mu^j \phi_T(K_t), \gamma^j)$, we have $\mathcal{O}(k_{t+1} k_t + k_t k_{t-1})$, provided that we have previously computed the gradient for the consecutive layer $t + 1$. Performing variational inference only on the last layer, i.e., ϕ_{T-1} requires $\mathcal{O}(k_T k_{T-1} h w)$ FLOP per sample.*

Our implementations exclusively use stride 1 convolutions for the layers indicated in Sec. 5, so $w_T = w_{T-1} = w_{T-2} =: w$, respectively $h_T = h_{T-1} = h_{T-2} =: h$. As before, we denote $n_t := h w k_t$, and regard $D\mathcal{L}^j$ as a $1 \times n_T$ matrix. Next, regard the matrix-vector multiplication to be performed in Eq. (49). Since for all $t \in [T]$ we have that ψ_t is linear in K_t , we regard $\nabla_{K_t} \psi_t$ as a matrix acting on the filter space $\mathbb{R}^{k_{t-1} \times k_t \times (2s_t + 1)^2}$. For $d \in [k_t]$, ψ_t^d only depends on K_t^d (see Eq. (46)), so $\nabla_{K_t} \psi_t$ only has at most $k_{t-1} \cdot (2s_t + 1)^2 \cdot n_t$ non-vanishing entries. Therefore, regard it as a $(n_t \times (k_{t-1} (2s_t + 1)^2))$ -matrix. We will now show that this matrix has $k_t (2s_t + 1)^2$ -sparse columns.

Let $c \in [k_t]$, $d \in [k_{t-1}]$, $p, q \in \{-s_t, \dots, s_t\}$, $a \in [h_t]$

Table 10. Upper bounds on FLOP and elementary function evaluations performed during the computation of $D\mathcal{L}^j$ (all contributions) and post processing for sampling-based uncertainty quantification (sampling pp) for N_{samp} inference samples.

	YOLOv3	Faster/Cascade R-CNN	RetinaNet
# FLOP $D\mathcal{L}^j$	$(9 + C)N_{\text{out}}$	$10N_{\text{out}}^{\text{RPN}} + (2 + 2C)N_{\text{out}}$	$(18 + 11C)N_{\text{out}}$
# FLOP sampling pp	$8N_{\text{out}}N_{\text{samp}}$	$(9 + 2C)N_{\text{out}}N_{\text{samp}}$	$8N_{\text{out}}N_{\text{samp}}$
# evaluations $D\mathcal{L}^j$	0	0	$2(1 + C)N_{\text{out}}$
# evaluations sampling pp	$(5 + C)N_{\text{out}}N_{\text{samp}}$	$(3 + C)N_{\text{out}}N_{\text{samp}}$	$(3 + C)N_{\text{out}}N_{\text{samp}}$

and $b \in [w_t]$. One easily sees from Eqs. (45) and (46) that

$$\frac{\partial}{\partial((K_t^d)_{pq}^d)}(\psi_t)_{ab}^d = (\phi_{t-1})_{a+p-s_t-1, b+q-s_t-1}^c, \quad (52)$$

where ϕ_{t-1}^c is considered to vanish for $a+p-s_t-1 \notin [h_t]$ and $b+q-s_t-1 \notin [w_t]$. Consistency with the definition of p and q requires that both the conditions

$$1 < a \leq 2s_t + 2, \quad 1 < b \leq 2s_t + 2 \quad (53)$$

are satisfied, which means that $(\nabla_{K_t}\psi_t)^d$ can only have $k_t(2s_t + 1)^2$ non-zero entries. Appealing to sparsity $\nabla_{K_T}\psi_T$ in Eq. (49) is then, effectively, a $((k_{T-1} \cdot (2s_T + 1)^2) \times (k_T \cdot (2s_T + 1)^2))$ -matrix, resulting in a FLOP count of

$$[2 \cdot k_T(2s_T + 1)^2 - 1] \cdot [k_{T-1} \cdot (2s_T + 1)^2] \quad (54)$$

for the multiplication $D\mathcal{L}^j \cdot \nabla_{K_T}\psi_T$ giving the claimed complexity considering that the computation of μ^j is $\mathcal{O}(k_T h w)$.

Next, we investigate the multiplication in Eq. (50), in particular the multiplication $D\mathcal{L}^j \cdot C^{K_T}$ as the same sparsity argument applies to $\nabla_{K_{T-1}}\psi_{T-1}$. First, for $t \in [T]$, regard C^{K_t} as a $(n_t \times n_{t-1})$ -matrix acting on a feature map $\phi \in \mathbb{R}^{n_{t-1}}$ from the left via

$$\begin{aligned} (C^{K_t}\phi)_{ab}^d &= \sum_{c=1}^{k_{t-1}} [(K_t^d)_c^d * \phi^c]_{ab} \\ &= \sum_{c=1}^{k_{t-1}} \sum_{m, n=-s_t}^{s_t} [(K_t^d)_c^d]_{s_t+1+m, s_t+1+n}(\phi^c)_{a+m, b+n}, \end{aligned} \quad (55)$$

where $d \in [k_t]$, $b \in [w_t]$ and $a \in [h_t]$ indicate one particular row in the matrix representation of C^{K_t} . From this, we see the sparsity of C^{K_t} , namely the multiplication result of row (d, a, b) acts on at most $k_{t-1} \cdot (2s_t + 1)^2$ components of ϕ_{t-1} (i.e., $k_{t-1}(2s_t + 1)^2$ -sparsity of the rows). Conversely, we also see that at most $k_t \cdot (2s_t + 1)^2$ convolution products $(C^{K_t}\phi)_{ab}^d$ have a dependency on one particular feature map pixel $(\phi^c)_{\bar{a}\bar{b}}$ (i.e., $k_t(2s_t + 1)^2$ -sparsity of the columns).

Now, let $t \in [T - 1]$ and assume that we have already computed the gradient

$$\begin{aligned} \nabla_{K_{t+1}}\mathcal{L} &= \nabla_{K_{t+1}}\ell_{t+1}(\phi_{t+1}(K_{t+1})) \\ &= D\ell_{t+1}|_{\phi_{t+1}} \cdot \alpha_{t+1}|_{\psi_{t+1}} \cdot \nabla_{K_{t+1}}\psi_{t+1}, \end{aligned} \quad (56)$$

then by backpropagation, i.e., Eq. (48), we obtain

$$\begin{aligned} \nabla_{K_t}\mathcal{L} &= \nabla_{K_t}[\ell_{t+1} \circ \alpha_{t+1} \circ \psi_{t+1}(\phi_t(K_t))] \\ &= D\ell_{t+1}|_{\phi_{t+1}} \cdot \alpha_{t+1}|_{\psi_{t+1}} \cdot C^{K_{t+1}} \cdot \\ &\quad \cdot D\alpha_t|_{\psi_t} \cdot \nabla_{K_t}\psi_t. \end{aligned} \quad (57)$$

Here, the first two factors have already been computed, hence we obtain a FLOP count for subsequently computing $\nabla_{K_t}\mathcal{L}$ of

$$\begin{aligned} &[2 \cdot k_{t+1}(2s_{t+1} + 1)^2 - 1] \cdot [k_t(2s_t + 1)^2] + \\ &+ [2 \cdot k_t(2s_t + 1)^2 - 1] \cdot [k_{t-1}(2s_t + 1)^2] \end{aligned} \quad (58)$$

via the backpropagation step from $\nabla_{K_{t+1}}\mathcal{L}$. The claim in Theorem 1 addressing Eq. (50), follows for $t = T - 1$ in Eq. (58).

Finally, we address the computational complexity for sampling-based uncertainty quantification methods with sampling on ϕ_{T-1} . This is applicable, e.g., for dropout on the last layer (as in our experiments) or a deep sub-ensemble [52] sharing the forward pass up to the last layer (note, that we do not use sub-ensembles in our experiments, but regular deep ensembles). Earlier sampling leads to far higher FLOP counts. Again, we ignore the cost of dropout itself as it is random binary masking together with a respective up-scaling/multiplication of the non-masked entries by a constant. The cost stated in Theorem 1 results from the residual forward pass $\phi_{T-1} \mapsto \phi_T = \alpha_T(C^{K_T} \cdot \phi_{T-1} + b_T)$ where we now apply previous results. Obtaining all n_T entries in the resulting sample feature map requires a total FLOP count of

$$2n_T k_{T-1}(2s_T + 1)^2 - 1 + n_T \quad (59)$$

as claimed, where we have considered the sparsity of C^{K_T} . The last term results from the bias addition.

Discussion. A large part of the FLOP required to compute gradient metrics results from the computation of the masks μ^j and the term $D\mathcal{L}^j$ for each relevant predicted box. In Tab. 10 we have treated the latter separately and found that, although the counts listed for $D\mathcal{L}^j$ apply to each separate box, sampling post-processing comes with considerable computational complexity as well. In that regard, we have similar costs for gradient metrics and sampling over the last network layer. Note in particular, that computing $D\mathcal{L}^j$ requires no new evaluation of elementary functions, as opposed to sampling. Once $D\mathcal{L}^j$ is computed for \tilde{y}^j , the last layer gradient can be computed in $\mathcal{O}(k_T k_{T-1})$ and every further gradient for layer V_t in $\mathcal{O}(k_{t+1} k_t + k_t k_{t-1})$. Each sample results in $\mathcal{O}(n_T k_{T-1})$ with sampling on ϕ_{T-1} . Sampling any earlier results in additional full convolution forward passes which also come with considerable computational costs. We note that sampling-based epistemic uncertainty can be computed in parallel with all N_{samp} forward passes being performed simultaneously. Gradient uncertainty metrics, in contrast, require one full forward pass for the individual gradients $\nabla_{K_t} \mathcal{L}(\mu^j \phi_T(K_t), \gamma^j)$ to be computed. Therefore, gradient uncertainty metrics experience a slight computational latency as compared to sampling methods. We argue that in principle, all following steps (computation of μ^j and $\nabla_{K_t} \mathcal{L}(\mu^j \phi_T(K_t), \gamma^j)$) can be implemented to run in parallel as no sequential order of computations is required. We have not addressed the computations of mapping the gradients to scalars from Eq. (3) which are roughly comparable to the cost of computing the sample std for sampling-based methods, especially once the sparsity of $D\mathcal{L}^j$ has been determined in the computation of $\nabla_{K_T} \mathcal{L}$. The latter also brings a significant reduction in FLOP (from n_T to $|\mu^j|$) which cannot be estimated more sharply, however. Since $D\mathcal{L}^j$ is sparse, multiplication from the right with $D\alpha_T|_{\psi_T}$ in Eqs. (49) and (50) for a leaky ReLU activation only leads to lower-order terms. The same terms were also omitted before in determining the computational complexity of sampling uncertainty methods. Also, for this consideration, we regard the fully connected layers used for bounding box regression and classification in the Faster/Cascade R-CNN RoI head as (1×1) -convolutions to stay in the setting presented here.

E. Further Numerical Results

E.1. Non-redundancy with output-based uncertainty

Gradient metrics show significant improvements when combined with output- or sampling-based uncertainty quantification methods (see Tab. 2 and Tab. 3). We show additional meta classification and meta regression results in Tab. 11 and in Tab. 12 to further illustrate this finding. First, in Tab. 11 we find that adding GS_{full} to the raw object de-

tection output features \tilde{y} performs similarly as the combination $\text{GS}_{\text{full}}+\text{MD}$. In fact, when directly comparing MD with \tilde{y} , we see consistently better results on \tilde{y} , even though MD contains \tilde{y} as co-variables. We attribute this finding to overfitting of the gradient boosting classifier and regression on MD. This suggests that the information in MD is mostly redundant with the network output features. Also, for combinations of one output-based uncertainty source (*i.e.*, one of MC, E and MD) we gain strong boosts, especially in meta regression (R^2). Note, that $\text{GS}_{\text{full}}+\text{E}_{\text{std}}$ is almost always the second-best model, even out-performing the purely output-based model $\text{MC}_{\text{std}}+\text{E}_{\text{std}}+\text{MD}$. We show meta classification and meta regression performance of the sampling-based epistemic uncertainty methods MC and E when we include sampling averages of all features in addition to standard deviations which also leads to significant boosts. Finally, we show an additional subset of GS_{full} consisting of one- and two-norms ($\{\|\cdot\|_1, \|\cdot\|_2\}$) of all gradients which we abbreviate by $\text{GS}_{\|\cdot\|_{1,2}}$. We notice significant gain of the latter to $\text{GS}_{\|\cdot\|_2}$, which shows that the one-norms $\|\cdot\|_1$ contains important predictive information. Moreover, GS_{full} is still significantly stronger than $\text{GS}_{\|\cdot\|_{1,2}}$, showing that the other uncertainty metrics in Eq. (3) lead to large performance boosts. Note that in almost all cases, combining MC dropout and deep ensemble metrics shows improvement over the single models even though both are epistemic (model) uncertainty. The two methods, therefore, do not contain the exact same information but still complement each other to some degree and are rather different approximations of epistemic uncertainty

For further illustration of our method, Tab. 12 shows additional meta classification and meta regression results for the architectures from Tab. 4. We find similar tendencies for the purely norm-based gradient model $\text{GS}_{\|\cdot\|_{1,2}}$ and see a significant degree of non-redundancy between gradient-based uncertainty and output-based uncertainty quantification methods. Note in particular, that MC stays roughly on par with the score baseline in terms of $AuROC$. We see significantly worse performance in terms of AP and meta regression (R^2). We attribute this to the anchor-based dropout sampling method which was also employed for the present architectures (in the case of Faster R-CNN, the aggregation approach is proposal-based).

Figure 8 shows the confidence violin plots of the score (left), GS_{full} (center) and $\text{GS}_{\text{full}}+\text{MC}+\text{E}+\text{MD}$ (right) conditioned on TP and FP predictions. The violin widths are normalized for increased width contrast. The score TP-violin shows especially large density at low confidences whereas the TP-violins of GS_{full} and $\text{GS}_{\text{full}}+\text{MC}+\text{E}+\text{MD}$ are less concentrated around the confidence $\hat{\tau} = 0$. Instead, they have mass shifted towards the medium confidence range (“neck”).

Table 11. Meta classification ($AuROC$ and AP) and meta regression (R^2) performance of baseline methods, variants of gradient metrics and different combinations of output-based uncertainty quantification methods with gradient metrics (mean \pm std). We also show the results of using the entire network output \tilde{y} for meta classification and regression, as well, as adding sampling means to standard deviation features for MC and E.

YOLOv3	Pascal VOC			COCO			KITTI		
	$AuROC$	AP	R^2	$AuROC$	AP	R^2	$AuROC$	AP	R^2
Score	90.68 \pm 0.06	69.56 \pm 0.12	48.29 \pm 0.04	82.97 \pm 0.04	62.31 \pm 0.05	32.60 \pm 0.02	96.55 \pm 0.04	96.87 \pm 0.03	78.83 \pm 0.05
Entropy	91.30 \pm 0.02	61.94 \pm 0.06	43.24 \pm 0.03	76.52 \pm 0.02	42.52 \pm 0.04	21.10 \pm 0.04	94.78 \pm 0.03	94.82 \pm 0.05	69.33 \pm 0.08
Energy	92.59 \pm 0.02	64.65 \pm 0.06	47.18 \pm 0.03	75.39 \pm 0.02	39.72 \pm 0.06	17.94 \pm 0.02	95.46 \pm 0.05	94.63 \pm 0.08	70.39 \pm 0.10
Full Softmax	93.81 \pm 0.06	72.08 \pm 0.15	53.86 \pm 0.11	82.91 \pm 0.06	58.65 \pm 0.10	36.95 \pm 0.13	97.10 \pm 0.02	96.90 \pm 0.04	78.79 \pm 0.12
Full output \tilde{y}	95.84 \pm 0.04	78.84 \pm 0.10	60.67 \pm 0.18	86.31 \pm 0.05	67.46 \pm 0.07	44.32 \pm 0.11	98.35 \pm 0.02	98.21 \pm 0.04	86.34 \pm 0.07
MC _{std}	96.72 \pm 0.02	78.15 \pm 0.09	61.63 \pm 0.15	89.04 \pm 0.02	64.94 \pm 0.11	43.85 \pm 0.09	95.43 \pm 0.04	94.11 \pm 0.12	75.09 \pm 0.13
MC _{std+mean}	97.42 \pm 0.02	84.18 \pm 0.09	68.33 \pm 0.16	90.40 \pm 0.03	72.63 \pm 0.07	52.38 \pm 0.07	98.43 \pm 0.03	98.28 \pm 0.04	86.86 \pm 0.09
E _{std}	96.87 \pm 0.02	77.86 \pm 0.11	61.48 \pm 0.07	88.97 \pm 0.02	64.05 \pm 0.12	43.53 \pm 0.13	97.98 \pm 0.03	97.69 \pm 0.04	84.29 \pm 0.12
E _{std+mean}	97.62 \pm 0.02	84.87 \pm 0.14	68.88 \pm 0.09	90.75 \pm 0.03	73.15 \pm 0.06	53.09 \pm 0.09	98.61 \pm 0.02	98.49 \pm 0.03	88.00 \pm 0.08
MC _{std+mean} +E _{std+mean}	97.69 \pm 0.02	85.30 \pm 0.11	69.60 \pm 0.13	91.15 \pm 0.03	73.85 \pm 0.05	54.12 \pm 0.09	98.61 \pm 0.01	98.49 \pm 0.02	87.95 \pm 0.10
MD	95.78 \pm 0.05	78.64 \pm 0.08	60.36 \pm 0.14	86.23 \pm 0.05	67.37 \pm 0.08	44.22 \pm 0.11	98.23 \pm 0.03	98.07 \pm 0.03	85.97 \pm 0.09
GS _{-l2}	94.76 \pm 0.03	74.86 \pm 0.10	58.05 \pm 0.13	84.90 \pm 0.02	61.49 \pm 0.08	38.77 \pm 0.04	97.30 \pm 0.05	96.82 \pm 0.10	81.11 \pm 0.14
GS _{-l1,2}	95.03 \pm 0.03	76.04 \pm 0.10	59.83 \pm 0.10	86.21 \pm 0.04	63.32 \pm 0.13	41.36 \pm 0.09	97.65 \pm 0.04	97.21 \pm 0.07	83.27 \pm 0.09
GS _{full}	95.80 \pm 0.04	78.57 \pm 0.11	62.50 \pm 0.11	86.94 \pm 0.04	66.96 \pm 0.06	44.90 \pm 0.09	98.04 \pm 0.02	97.81 \pm 0.04	85.28 \pm 0.07
GS _{full} + \tilde{y}	96.51 \pm 0.018	81.20 \pm 0.09	65.24 \pm 0.16	87.54 \pm 0.04	69.05 \pm 0.07	47.67 \pm 0.09	98.57 \pm 0.03	98.47 \pm 0.04	87.83 \pm 0.08
GS _{full} +MC _{std}	97.65 \pm 0.01	85.12 \pm 0.06	70.30 \pm 0.08	90.76 \pm 0.02	72.50 \pm 0.08	52.71 \pm 0.07	98.35 \pm 0.04	98.16 \pm 0.04	86.48 \pm 0.11
GS _{full} +E _{std}	97.85 \pm 0.02	85.90 \pm 0.15	71.22 \pm 0.07	91.27 \pm 0.03	73.44 \pm 0.06	54.17 \pm 0.06	98.64 \pm 0.02	98.49 \pm 0.03	88.34 \pm 0.10
GS _{full} +MD	96.46 \pm 0.04	81.00 \pm 0.16	65.08 \pm 0.14	87.51 \pm 0.02	68.98 \pm 0.08	47.63 \pm 0.10	98.53 \pm 0.03	98.42 \pm 0.04	87.69 \pm 0.06
MC _{std} +E _{std} +MD	97.66 \pm 0.02	85.13 \pm 0.12	69.38 \pm 0.11	91.14 \pm 0.02	73.82 \pm 0.05	54.07 \pm 0.08	98.56 \pm 0.03	98.45 \pm 0.03	87.78 \pm 0.11
GS _{full} +MC _{std} +E _{std} +MD	97.95 \pm 0.02	86.69 \pm 0.09	72.26 \pm 0.08	91.65 \pm 0.03	74.88 \pm 0.07	56.14 \pm 0.11	98.74 \pm 0.02	98.62 \pm 0.01	88.80 \pm 0.07

Table 12. Meta classification ($AuROC$ and AP) and meta regression (R^2) performance of baseline methods, variants of gradient metrics and combinations of output- and gradient-based metrics for different object detection architectures (mean \pm std).

	Pascal VOC			COCO			KITTI		
	$AuROC$	AP	R^2	$AuROC$	AP	R^2	$AuROC$	AP	R^2
Faster R-CNN									
Score	89.77 \pm 0.05	67.71 \pm 0.03	39.94 \pm 0.02	83.82 \pm 0.03	64.14 \pm 0.03	40.50 \pm 0.01	96.53 \pm 0.05	93.29 \pm 0.02	72.29 \pm 0.02
MC	89.99 \pm 0.06	44.22 \pm 0.26	23.70 \pm 0.17	85.80 \pm 0.03	40.48 \pm 0.12	23.56 \pm 0.09	93.39 \pm 0.07	67.82 \pm 0.24	40.09 \pm 0.17
MD	94.43 \pm 0.02	71.18 \pm 0.06	47.92 \pm 0.09	91.31 \pm 0.02	64.73 \pm 0.05	44.41 \pm 0.04	98.86 \pm 0.03	94.31 \pm 0.05	79.92 \pm 0.04
GS _{-l2}	91.04 \pm 0.07	61.66 \pm 0.15	44.88 \pm 0.05	89.80 \pm 0.03	61.16 \pm 0.06	44.93 \pm 0.04	98.75 \pm 0.02	93.01 \pm 0.05	81.54 \pm 0.05
GS _{-l1,2}	94.91 \pm 0.04	67.73 \pm 0.10	56.70 \pm 0.06	90.64 \pm 0.03	62.53 \pm 0.07	48.27 \pm 0.03	98.97 \pm 0.03	93.89 \pm 0.07	84.04 \pm 0.04
GS _{full}	95.88 \pm 0.05	68.74 \pm 0.13	59.40 \pm 0.03	91.38 \pm 0.03	63.31 \pm 0.07	50.44 \pm 0.04	99.20 \pm 0.01	94.60 \pm 0.07	86.31 \pm 0.07
GS _{full} +MC	96.59 \pm 0.03	71.31 \pm 0.08	60.74 \pm 0.07	92.09 \pm 0.02	64.59 \pm 0.06	51.09 \pm 0.04	99.34 \pm 0.02	95.24 \pm 0.05	86.85 \pm 0.04
GS _{full} +MD	96.77 \pm 0.05	73.60 \pm 0.07	63.64 \pm 0.08	92.30 \pm 0.02	65.67 \pm 0.05	52.30 \pm 0.04	99.37 \pm 0.02	95.38 \pm 0.05	87.46 \pm 0.05
GS _{full} +MC+MD	96.72 \pm 0.04	73.51 \pm 0.10	63.02 \pm 0.03	92.30 \pm 0.01	65.77 \pm 0.06	52.21 \pm 0.04	99.35 \pm 0.02	95.37 \pm 0.03	86.99 \pm 0.07
RetinaNet									
Score	87.53 \pm 0.03	66.30 \pm 0.05	40.43 \pm 0.01	84.95 \pm 0.04	68.58 \pm 0.01	39.88 \pm 0.02	95.91 \pm 0.02	89.93 \pm 0.02	73.44 \pm 0.02
MC	72.90 \pm 0.08	27.39 \pm 0.11	14.17 \pm 0.12	76.96 \pm 0.04	43.54 \pm 0.06	19.46 \pm 0.06	88.13 \pm 0.06	71.19 \pm 0.10	50.51 \pm 0.12
MD	89.57 \pm 0.04	68.43 \pm 0.08	50.27 \pm 0.10	85.09 \pm 0.01	68.32 \pm 0.06	42.45 \pm 0.12	96.19 \pm 0.03	90.13 \pm 0.04	77.53 \pm 0.08
GS _{-l2}	87.86 \pm 0.04	64.35 \pm 0.06	46.19 \pm 0.05	81.62 \pm 0.04	63.95 \pm 0.03	38.01 \pm 0.04	95.93 \pm 0.03	90.03 \pm 0.05	79.17 \pm 0.04
GS _{-l1,2}	88.77 \pm 0.06	65.40 \pm 0.05	49.64 \pm 0.06	83.53 \pm 0.05	65.88 \pm 0.07	41.96 \pm 0.05	96.47 \pm 0.04	90.50 \pm 0.03	81.35 \pm 0.05
GS _{full}	91.58 \pm 0.04	68.32 \pm 0.06	57.23 \pm 0.07	85.59 \pm 0.02	67.93 \pm 0.04	47.74 \pm 0.06	97.26 \pm 0.03	91.51 \pm 0.07	84.47 \pm 0.04
GS _{full} +MC	92.54 \pm 0.03	70.65 \pm 0.06	61.73 \pm 0.04	86.87 \pm 0.03	69.42 \pm 0.03	50.63 \pm 0.07	97.52 \pm 0.02	91.98 \pm 0.06	85.08 \pm 0.04
GS _{full} +MD	92.99 \pm 0.03	72.30 \pm 0.08	64.32 \pm 0.07	87.15 \pm 0.05	70.16 \pm 0.07	51.07 \pm 0.09	97.61 \pm 0.02	92.26 \pm 0.05	85.73 \pm 0.09
GS _{full} +MC+MD	92.95 \pm 0.03	72.33 \pm 0.07	63.44 \pm 0.06	87.20 \pm 0.04	70.21 \pm 0.03	51.38 \pm 0.09	97.63 \pm 0.01	92.30 \pm 0.03	85.64 \pm 0.08
Cascade R-CNN									
Score	95.70 \pm 0.04	79.62 \pm 0.10	57.90 \pm 0.09	94.11 \pm 0.01	81.36 \pm 0.02	56.32 \pm 0.02	98.67 \pm 0.02	95.81 \pm 0.04	83.31 \pm 0.03
MD	96.32 \pm 0.05	82.11 \pm 0.12	63.62 \pm 0.12	94.12 \pm 0.03	81.60 \pm 0.05	58.84 \pm 0.04	99.18 \pm 0.01	96.60 \pm 0.05	86.22 \pm 0.08
GS _{-l2}	96.46 \pm 0.05	76.94 \pm 0.19	61.56 \pm 0.12	93.30 \pm 0.02	76.40 \pm 0.06	54.13 \pm 0.06	99.19 \pm 0.01	95.83 \pm 0.06	85.80 \pm 0.06
GS _{-l1,2}	96.54 \pm 0.06	78.19 \pm 0.22	62.82 \pm 0.15	93.63 \pm 0.02	77.95 \pm 0.06	56.24 \pm 0.05	99.23 \pm 0.01	96.07 \pm 0.05	86.33 \pm 0.06
GS _{full}	96.66 \pm 0.05	78.97 \pm 0.19	63.94 \pm 0.13	93.97 \pm 0.02	79.17 \pm 0.09	57.86 \pm 0.05	99.34 \pm 0.01	96.48 \pm 0.04	87.39 \pm 0.08
GS _{full} +MD	97.24 \pm 0.05	84.11 \pm 0.13	69.78 \pm 0.13	94.78 \pm 0.02	82.53 \pm 0.05	62.13 \pm 0.05	99.48 \pm 0.01	97.27 \pm 0.04	89.59 \pm 0.04

E.2. Calibration of meta classifiers

For sake of completeness, we list in Tab. 13 the calibration metrics ECE , MCE and ACE defined in Appendix A

Table 13. Expected (ECE , [38]), maximum (MCE , [38]) and average (ACE , [39]) calibration errors per confidence model over 10-fold cv (mean \pm std).

	Pascal VOC			COCO			KITTI		
YOLOv3	ECE	MCE	ACE	ECE	MCE	ACE	ECE	MCE	ACE
Score	0.040	0.252	0.114	0.0327	0.050	0.034	0.068	0.348	0.227
Entropy	0.002 ± 0.001	0.021 ± 0.010	0.007 ± 0.003	0.002 ± 0.001	0.028 ± 0.020	0.007 ± 0.003	0.005 ± 0.001	0.033 ± 0.010	0.011 ± 0.003
Energy Score	0.001 ± 0.001	0.015 ± 0.007	0.005 ± 0.002	0.002 ± 0.001	0.021 ± 0.003	0.008 ± 0.001	0.006 ± 0.002	0.034 ± 0.010	0.013 ± 0.005
Full Softmax	0.003 ± 0.000	0.028 ± 0.006	0.010 ± 0.002	0.003 ± 0.001	0.018 ± 0.003	0.007 ± 0.001	0.008 ± 0.001	0.048 ± 0.010	0.018 ± 0.002
MC	0.004 ± 0.000	0.033 ± 0.006	0.014 ± 0.002	0.004 ± 0.001	0.025 ± 0.003	0.010 ± 0.001	0.011 ± 0.001	0.036 ± 0.010	0.013 ± 0.002
E	0.003 ± 0.000	0.025 ± 0.005	0.010 ± 0.002	0.004 ± 0.001	0.022 ± 0.003	0.010 ± 0.001	0.013 ± 0.001	0.062 ± 0.010	0.028 ± 0.004
MD	0.003 ± 0.000	0.040 ± 0.009	0.012 ± 0.001	0.005 ± 0.001	0.033 ± 0.005	0.014 ± 0.001	0.012 ± 0.001	0.074 ± 0.020	0.028 ± 0.005
GS _{1-l2}	0.003 ± 0.000	0.036 ± 0.007	0.014 ± 0.001	0.002 ± 0.000	0.013 ± 0.004	0.005 ± 0.001	0.008 ± 0.001	0.054 ± 0.010	0.022 ± 0.003
GS _{full}	0.005 ± 0.000	0.055 ± 0.002	0.021 ± 0.003	0.005 ± 0.001	0.039 ± 0.003	0.015 ± 0.001	0.012 ± 0.001	0.078 ± 0.020	0.034 ± 0.006
MC+E+MD	0.005 ± 0.001	0.049 ± 0.010	0.020 ± 0.003	0.005 ± 0.000	0.031 ± 0.006	0.014 ± 0.001	0.014 ± 0.001	0.076 ± 0.010	0.034 ± 0.005
MC+E+MD+GS _{full}	0.005 ± 0.000	0.061 ± 0.010	0.024 ± 0.003	0.006 ± 0.000	0.042 ± 0.004	0.018 ± 0.001	0.015 ± 0.001	0.106 ± 0.020	0.043 ± 0.006
Faster R-CNN									
Score	0.050	0.427	0.232	0.075	0.212	0.138	0.036	0.283	0.114
MD	0.003 ± 0.000	0.039 ± 0.007	0.013 ± 0.002	0.004 ± 0.000	0.020 ± 0.003	0.009 ± 0.001	0.009 ± 0.001	0.079 ± 0.020	0.029 ± 0.004
GS _{full}	0.004 ± 0.000	0.027 ± 0.007	0.011 ± 0.001	0.004 ± 0.001	0.024 ± 0.003	0.009 ± 0.001	0.010 ± 0.001	0.084 ± 0.020	0.035 ± 0.004
MD+GS _{full}	0.005 ± 0.000	0.044 ± 0.007	0.018 ± 0.002	0.006 ± 0.001	0.029 ± 0.006	0.012 ± 0.001	0.011 ± 0.001	0.088 ± 0.010	0.037 ± 0.004
RetinaNet									
Score	0.068	0.212	0.123	0.089	0.192	0.106	0.027	0.097	0.043
MD	0.003 ± 0.000	0.031 ± 0.008	0.011 ± 0.002	0.005 ± 0.001	0.022 ± 0.004	0.009 ± 0.001	0.003 ± 0.000	0.044 ± 0.006	0.016 ± 0.002
GS _{full}	0.003 ± 0.000	0.044 ± 0.009	0.014 ± 0.001	0.005 ± 0.000	0.031 ± 0.006	0.012 ± 0.001	0.005 ± 0.001	0.060 ± 0.010	0.022 ± 0.004
MD+GS _{full}	0.005 ± 0.000	0.064 ± 0.008	0.024 ± 0.002	0.007 ± 0.001	0.032 ± 0.004	0.015 ± 0.001	0.006 ± 0.000	0.070 ± 0.010	0.028 ± 0.003
Cascade R-CNN									
Score	0.020	0.219	0.090	0.029	0.082	0.042	0.013	0.188	0.078
MD	0.003 ± 0.000	0.021 ± 0.006	0.007 ± 0.002	0.003 ± 0.000	0.019 ± 0.007	0.006 ± 0.001	0.002 ± 0.000	0.038 ± 0.010	0.016 ± 0.005
GS _{full}	0.005 ± 0.000	0.032 ± 0.010	0.012 ± 0.002	0.003 ± 0.000	0.017 ± 0.003	0.007 ± 0.001	0.003 ± 0.000	0.052 ± 0.010	0.020 ± 0.004
MD+GS _{full}	0.005 ± 0.000	0.034 ± 0.008	0.014 ± 0.002	0.004 ± 0.000	0.025 ± 0.004	0.010 ± 0.001	0.003 ± 0.000	0.046 ± 0.009	0.019 ± 0.003

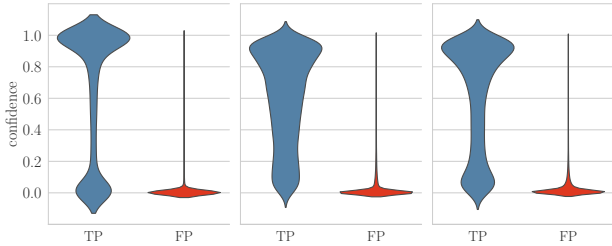


Figure 8. Confidence violin plots divided into TP and FP for Score (left), GS_{full} (center) and GS_{full}+MC+E+MD (right). Model: YOLOv3, dataset: Pascal VOC evaluation split.

for score and meta classifiers for all object detectors on all three datasets investigated in Sec. 5. All calibration metrics are in line with the results from Sec. 5 with meta classifiers being always better calibrated than the score by at least half an order of magnitude in any calibration metric. See also Fig. 9 for the additional reliability diagrams for MC, E and MC+E+MDGS_{full} which extends Fig. 3. The ECE metric is comparatively small for all meta classifiers and, therefore, insensitive and harder to interpret than MCE and ACE . As was argued in [39], the former is also less informative as bin-wise accuracy is weighted with the bin counts. In Tab. 13 we can see a weakly increasing trend of calibration errors in the meta classifiers due to overfitting on the increasing number of co-variables. All meta classifiers are well-calibrated across the board.

E.3. Meta regression scatter plots

We underline the meta regression results obtained in Sec. 5 and Appendix E by showing samples of predicted IoU values over their true IoU in Fig. 10. The samples are the results of one cross-validation split from Tab. 3 and we indicate the diagonal of optimal regression with a dashed line in each panel. Note that the x -axis shows the true IoU values and we indicate the uncertainty quantification method below each panel plot at a label. The y -axis shows the predicted IoU for each method. We find a large cluster for the score with low score but medium to high true IoU (from 0.1 to 0.8), the right-most part of which (predicted $IoU \geq 0.5$) are false negative predictions. In this regard, we refer again to Fig. 6 where FNs such as these become very apparent. Moreover, the score indicates very little correlation with the true IoU for true $IoU \geq 0.6$ where there are numerous samples with a score between 0.4 and 0.6.

In contrast, the meta regression models show striking amounts of FPs (true IoU equal to 0 and, e.g., prediction $\iota \geq 0.3$). This phenomenon seems especially apparent for Monte Carlo dropout uncertainty. The meta regression models MD, GS_{full} and GS_{full}+MC+E+MD show fits that are comparatively close to the optimal diagonal which is in line with the determined regression performance R^2 between 0.81 and 0.89 in Tab. 3.

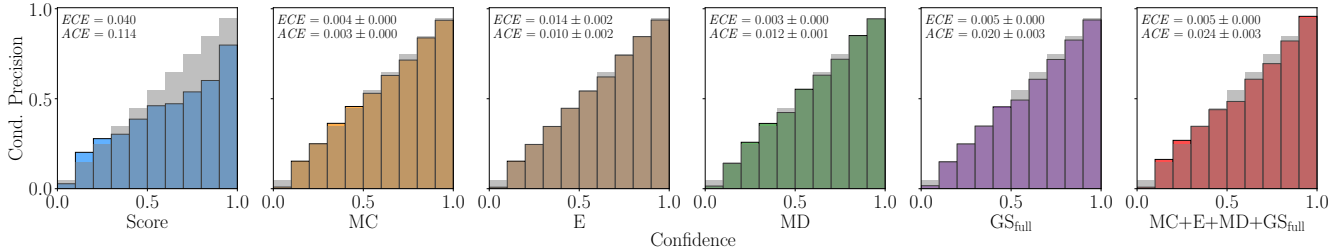


Figure 9. Reliability diagrams for the Score and meta classifiers based on different epistemic uncertainty metrics of the YOLOv3 architecture on the KITTI dataset. See Tab. 13 for calibration errors of all meta classification models investigated in Sec. 5.

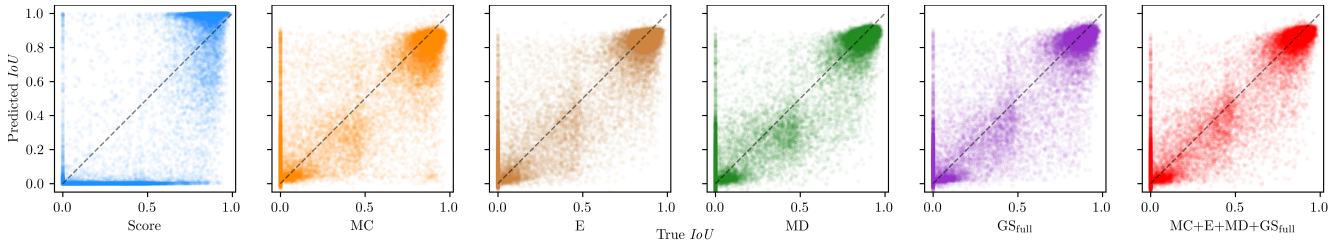


Figure 10. Scatter plots for samples of Score and meta regression based on MC dropout, gradient metrics G and the combination model G+MD+MC. We draw the optimal diagonal for reference. Model: YOLOv3, dataset: KITTI evaluation split.

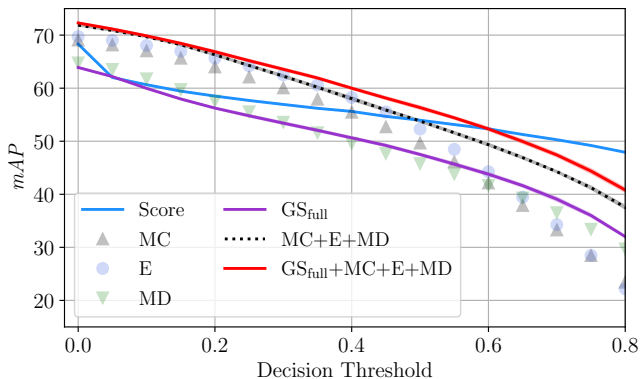


Figure 11. Score baseline and MetaFusion mAP for the VOC evaluation dataset for YOLOv3 from 10-fold cv.

E.4. MetaFusion on Pascal VOC.

In addition to the mAP plot in Fig. 5 we show the COCO evaluation metrics AP , AP_{50} , AP_{75} , AP_S , AP_M , AP_L in Tab. 14 at a confidence threshold of 0.05. We see that MD performs strong across different metrics and the combined models consistently outperform the single metric models. Gradient uncertainty models perform well for bounding boxes in the S and L categories with an improvement of 2.75 pts. over the Score baseline in AP_S . Adding gradient uncertainty to MC+E+MD yields 0.22 additional pts. which is, however, within the 1 sigma overlap. Note that the Score model is the second best in terms of AP_{75} , however, all meta classification models are fitted with a

(meta) ground truth, where a prediction is classified as TP at the IoU threshold 0.5. Fitting a meta classifiers at an IoU threshold of 0.75 is likely to perform better in the AP_{75} metric.

We also show MetaFusion plots analogous to Fig. 5 also for YOLOv3 on the VOC2007 test split in Fig. 11. The qualitative behavior is similar to the one presented for the KITTI dataset in Sec. 5, however, we do not see significant improvements by utilizing the purely gradient-based model GS_{full} . Also, MC performs much stronger than on the KITTI dataset and is almost on par with E. The combined models MC+E+MD and GS_{full} +MC+E+MD perform best, achieving higher maximum mAP than the score baseline by around 4 pts. Note also, that there is a larger gap between MC+E+MD and GS_{full} +MC+E+MD for thresholds ≥ 0.2 indicating gain from adding gradient uncertainty. We point out that the score baseline shows a similar kink as in Fig. 5 indicating a large amount of true predictions at low score values $\hat{s} \leq 0.05$.

Table 14. COCO AP metrics for the meta fusion models in Fig. 5 at a confidence threshold of $\varepsilon_s = 0.05$.

	AP	AP_{50}	AP_{75}	AP_S	AP_M	AP_L
Score	58.9	88.25	<u>68.27</u>	50.80	60.00	63.91
MC	57.58 ± 0.18	89.46 ± 0.19	65.55 ± 0.30	50.47 ± 0.83	59.12 ± 0.14	61.84 ± 0.28
E	<u>59.07 ± 0.07</u>	90.40 ± 0.07	67.92 ± 0.12	52.37 ± 0.51	<u>60.79 ± 0.09</u>	63.15 ± 0.17
MD	59.84 ± 0.07	91.59 ± 0.13	68.62 ± 0.08	52.74 ± 0.16	60.95 ± 0.08	64.72 ± 0.20
GS _{full}	59.00 ± 0.09	<u>90.65 ± 0.12</u>	67.47 ± 0.23	53.53 ± 0.16	59.80 ± 0.14	<u>63.92 ± 0.19</u>
MC+E+MD	60.27 ± 0.11	91.91 ± 0.10	69.29 ± 0.21	53.33 ± 0.32	61.40 ± 0.13	64.99 ± 0.15
MC+E+MD+GS _{full}	60.35 ± 0.09	91.89 ± 0.09	69.41 ± 0.18	53.55 ± 0.20	61.43 ± 0.14	65.05 ± 0.14